Ocean Engineering 278 (2023) 114201

Contents lists available at ScienceDirect

Ocean Engineering

journal homepage: www.elsevier.com/locate/oceaneng

ν-gap metric based multi-model predictive control of an ocean current turbine system with blade pitch failures☆

E. Baris Ondes [a,*], Cornel Sultan [a], Arezoo Hasankhani [b], James H. VanZwieten [b], Nikolaos I. Xiros [c]

[a] Virginia Tech, 460 Old Turner St., Blacksburg, 24061, VA, USA
[b] Florida Atlantic University, 777 Glades Road, Boca Raton, 33431, FL, USA
[c] University of New Orleans, 2000 Lakeshore Drive, New Orleans, 70148, LA, USA

ARTICLE INFO

Keywords:
Multi-model predictive control
Marine renewable energy
Fault-tolerant control
ν-gap metric
Ocean current turbine

ABSTRACT

In this article, a method of combining multiple linear models is developed and used by an advanced model predictive control algorithm for ocean current turbine flight control. The developed model bank consists of faulty and healthy linear models created for the ocean current turbine system. Each linear model is used to compute individual control actions using the model predictive control framework, which are combined to generate the aggregate control action that is applied to the system. A weighted average defined by the ν-gap distance between the current linear approximation of system dynamics and each individual linear system is used to compute the aggregate control action. The multi-model predictive control strategy is applied to control the ocean current turbine to mitigate performance degradation that may occur due to failures in the system. The proposed control framework's effectiveness is shown with the renewable power generation improvement during a faulty case.

1. Introduction

Ocean currents are global resources of clean energy that can be harvested using adequately designed and managed ocean current turbines (OCT), i.e. marine current turbines (MCT). According to Haas (2013), the Gulf Stream is a significant marine hydrokinetic energy source off the eastern coast of the United States, with an average power that can be generated along the coastline from Florida to North Carolina calculated at 18.6 GW. The optimal operation of OCTs requires that they are placed relatively far from the ocean shore and close to the water surface, ideally within the top 100 m of the water column. The highest power density regions are found on the western boundaries of the world's oceans and vary significantly with geographic location. For example, the highest power density is estimated to be 3.0 kW/m^2 at a depth of 50 m off the southeast coast of the U.S. (Lund et al., 2006); the maximum average power densities are estimated to be 2.15 kW/m^2 and 2.17 kW/m^2 at 20 m depth off Japan and South Africa (Mikhailov, 2002; Bryden et al., 2005). Placing OCTs at an ideal operating location, where the current is strongest, brings multiple challenges. These challenges include those associated with OCTs being moored to the ocean floor, as mooring systems (e.g., cables) introduce significant difficulties such as minimizing OCTs motions, placing and maintaining OCTs at the ideal locations, etc.

The ideal operating location for OCTs makes frequent failure-induced maintenance actions undesirable because of access limitations and the cost of offshore operations. Therefore, to be cost-effective, OCTs should operate without human intervention for long periods. Also, due to the operational environment, OCTs will be subjected to various perturbations, including large disturbances caused by extreme weather events (Hasankhani et al., 2021b). Modeling uncertainties are inevitable because of the environmental hydrodynamics, the complexity of the device (OCT), and the influence of the mooring system on the OCT dynamics. These challenges require an advanced feedback control system, which can rapidly react to diverse perturbations, reject disturbances, including those with large magnitudes, and manage system failures. Such control systems have not been investigated for OCTs yet. The OCT control literature is generally limited to stabilizing flight control systems that use a single linear model of the ideal (i.e., healthy, non-faulty) OCT. Fault-tolerant control of the OCTs studies are limited

☆ The authors would like to thank the National Science Foundation (NSF) for their valuable ongoing support in this research within the framework of grants ECCS-1809404/1809164/1809182 'Collaborative Research: Design and Control of Networked Offshore Hydrokinetic Power-Plants with Energy Storage'.

* Corresponding author.
E-mail addresses: ondes@vt.edu (E.B. Ondes), csultan@vt.edu (C. Sultan), ahasankhani2019@fau.edu (A. Hasankhani), jvanzwi@fau.edu (J.H. VanZwieten), nxiros@uno.edu (N.I. Xiros).

https://doi.org/10.1016/j.oceaneng.2023.114201
Received 10 November 2022; Received in revised form 5 March 2023; Accepted 11 March 2023
Available online 18 April 2023

to electronic failures in the system (Pham et al., 2018) and do not account for structural failures. There exist some published works on detecting and classifying failures in the rotor blade pitch angles using neural networks (Freeman et al., 2021, 2022), but they do not propose any fault-tolerant control framework. They can be used in failure mitigation algorithms (e.g. the one proposed in this work) to provide the system with information on the severity of the rotor blade pitch faults. The existing OCT control systems are implicitly limited in their capability to manage system failures, especially structural ones, as well as large and diverse perturbations. Some works in OCT control literature are briefly reviewed next.

PID/Bang-Bang, LQR/PID/Bang-Bang, and LQG/PID/Bang-Bang approaches were developed for the control of OCTs that use wingtips and canard fins as actuators, to primarily control some of the system's states, such as depth and orientation, and to maximize energy generation from ocean currents (VanZwieten et al., 2006). In Ngo et al. (2021), cyclic blade pitch angle control was introduced in OCT feedback control, in addition to the electromagnetic rotor torque control. A single OCT linear model was used in conjunction with a stochastic linear control method (output variance constrained control) to minimize control energy subject to variance constraints on deviations from the nominal values of lateral and vertical OCT inertial coordinates and rotor angular speed. It was ascertained that output variance-constrained (OVC) control can rapidly restore a perturbed OCT to the ideal operating condition. Also, practical OVC limits can be satisfied with small control energy while avoiding a blade stall. When position and linear velocity sensors fail or these measurements are missing, the performance of OCT equipped with an OVC controller degrades significantly. This was the only work that addressed failures of OCT by assessing its performance when sensor failure occurs. Control design was not performed to mitigate these failures.

Recently, Model Predictive Control (MPC) was used to control OCT systems, using as control inputs the blade pitch angle and the generator torque. MPC was used both in twin turbines (Sato et al., 2021) and in OCTs with only one rotor (Ngo et al., 2017). Additionally, MPC was compared with deep reinforcement learning (DRL) to obtain the optimized depth of an OCT to maximize the harnessed power from a lifting surface controlled OCT in Hasankhani et al. (2021a) and a buoyancy controlled OCT in Hasankhani et al. (2022c). In the most recent work, MPC was also utilized together with DRL, a co-design method, where MPC was used for path tracking of the OCT to follow the reference path under different shear profiles successfully, while DRL was utilized to find the optimal path in an uncertain ocean environment in a real-time manner (Hasankhani et al., 2022b). MPC was further applied to address path planning for the OCT, where a spatiotemporal neural network was employed to model the ocean current velocity (Hasankhani et al., 2022a). In this article, we develop an advanced control algorithm based on MPC for an OCT system with control inputs, including the rotor torque and the variable buoyancy of the buoyancy system as presented in Hasankhani et al. (2021b). Note that a similar variable buoyancy design was used in the world's first OCT system deployed successfully in August 2017 in open ocean currents (Ueno et al., 2018a).

Here, we present a method for combining multiple linear models applied using an advanced MPC algorithm for an OCT system to mitigate performance degradation that may occur due to the faults in the system. For this purpose, a model bank consisting of faulty (due to blade pitch fault) and healthy linear models are created for the OCT using the nonlinear model at the same operating condition. Each linear model is used to compute individual optimal control actions (i.e., inputs), which are then combined to generate the aggregate control action that is applied to the system. To combine these individual optimal control inputs, a weight function (Du and Johansen, 2014) is used where the weight for each input is defined by the ν-gap distance (Vinnicombe, 1999) between the current linear approximation of the system dynamics (i.e., which corresponds to the OCT state and condition at the current time instant) and the nominal, ideal, operating condition. Depending on the OCT's state and condition (i.e. healthy or faulty), a subset of the model bank is used to compute the aggregate control action with the Multi-Model Predictive Control (MMPC) strategy. The proposed algorithm has the benefit of being able to control the system with structural failures in the rotor. The MPC strategy is applied to update the control actions for each linear system at each time step, taking into account many constraints for the multi-input multi-output OCT system. To obtain the optimal control actions, an optimization problem is solved, which is formulated to follow the desired (i.e., reference) states with minimum control energy to keep the power consumption as low as possible.

The contributions of this work are summarized as follows:

1. A multi-model predictive control algorithm for nonlinear systems is proposed, and its effectiveness is presented with an application on an ocean current turbine system with pitch blade faults.
2. The ν-gap metric is used to identify the similarities between the models inside a model bank consisting of linear discrete-time models generated for different conditions from a high-fidelity, nonlinear model. Then, the pitch blade faults are isolated by making use of this model bank.
3. The proposed method provides a satisfactory trajectory following results for the OCT system, and with this proposed MMPC, even under faulty conditions, the system displays a behavior similar to that of a single MPC under non-faulty (healthy) conditions as given in Hasankhani et al. (2022b). This increases the power generated by the system significantly since the depth of the turbine is critical to exploit optimally the fastest ocean current flow.

In Section 2, the details about the OCT system are given, and changes from the previous model's actuators (i.e., the model used in Ngo et al., 2021) are described. The linearization of the nonlinear OCT model and the process of faulty model creation are then explained in Section 2. In Section 3, the details of the MMPC strategy are explained. In Section 4, an application of MMPC control on the OCT system is presented. Conclusions are given in Section 5.

2. Ocean current turbine system

The investigated OCT is designed for operation in the Gulf Stream off Florida's East Coast (Hasankhani et al., 2021b). This system has a total mass of 4.98×10^5 kg without considering ballast water. A variable buoyancy tank is utilized that has two separate buoyancy chambers, each of which can hold 3.20×10^4 kg of water. Assuming empty ballast chambers, the moments of inertia of the OCT system are $I_x = 1.35\times10^7$ kg m^3, $I_y = 4.74\times10^7$ kg m^3, and $I_z = 3.45\times10^7$ kg m^3 (see details of numerical modeling of the OCT system in Intelligent and Group, 2021). In this section, a nonlinear model of this OCT, its actuator model, and a rotor fault model are presented.

2.1. Nonlinear OCT model

A summary of the nonlinear mathematical model of the OCT system is given next (see Hasankhani et al., 2021b; VanZwieten et al., 2013 for details). The OCT, depicted in Fig. 1, is designed with a rated power of 700 kW and consists of a 20 m diameter 3-bladed variable pitch rotor, a single variable buoyancy tank separated internally into two variable buoyancy chambers, a main body, and a 607 m mooring cable that attaches the OCT to the ocean floor at a depth of 325 m (Hasankhani et al., 2021b). The system roughly follows the basic design of prototypes from IHI Corp. (Ueno et al., 2018b) and the University of Naples (Coiro et al., 2017), with the variable buoyancy chambers sized such that the OCT operates at a depth of 50 m, if they are half-filled with ballast water, when the ocean current speed is 1.6 m/s. A seven degree-of-freedom (DOF) model was developed to

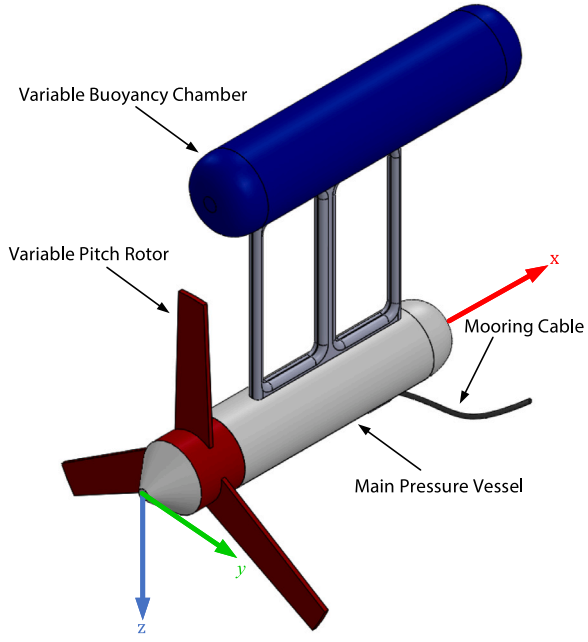

Fig. 1. Schematic of the buoyancy controlled OCT (Hasankhani et al., 2021b).

simulate this system (Hasankhani et al., 2021b) and is used here. This model includes the OCT rigid body dynamics, as well as the mooring cable dynamics and environmental effects, as briefly described next.

The rotor model was developed to calculate forces for both axial and non-axial flow fields that vary in space and time (VanZwieten et al., 2016). Rotor airfoils vary along the blade length from nearly cylindrical at the hub to an FX-83 W airfoil with a thickness ratio of 21% at 20% of the rotor radius and FX-83 W with a thickness ratio of 10.8% at the blade tip (see VanZwieten et al., 2016 for details). To calculate hydrodynamic forces on the rotor blades, an unsteady version of the Blade Element Momentum (BEM) model was used (see VanZwieten et al., 2013 for details). Besides the rotor forces, the hydrodynamic forces that act on the main body, variable buoyancy tank, and cable elements were included in the model. In addition to these hydrodynamic forces, the effects of gravity, buoyancy, and elastic cable forces were also included (VanZwieten et al., 2013).

This ocean current turbine is modeled as having a single 607 m long mooring cable with a diameter of 0.16 m (Hasankhani et al., 2021b). This cable is modeled as having a displaced mass of 20.6 kg/m, and a mass of 46 kg/m is assumed based on the average density of a double-armor umbilical suggested for offshore wind in Rentschler et al. (2019). This cable is modeled using the finite element lumped mass cable modeling approach as described in VanZwieten et al. (2013) and originally in Radanovic and Driscoll (2002). It was found, via nonlinear simulations, that five cable elements are sufficient to describe the OCT dynamics accurately (Vanrietvelde, 2009). Using a larger number of cable elements has negligible effects on predicted system performance but increases computational cost.

2.1.1. Kinematic and coordinate frames

The following coordinate frames are utilized by the OCT numerical simulation: the inertial coordinate frame ($\mathcal{T}_I$), the body-fixed coordinate frame ($\mathcal{T}_B$), the momentum mesh coordinate frame ($\mathcal{T}_M$), the shaft coordinate frame ($\mathcal{T}_S$), and multiple rotor blade coordinate frames ($\mathcal{T}_R$). The frame ($\mathcal{T}_I$) is located at the mean ocean level, with its x-axis pointing north, the y-axis pointing east, and the z-axis pointing vertically downwards. The origin of ($\mathcal{T}_B$) is placed at the location where the shaft is connected to the rotor blade, with its x-axis pointing towards the nose and co-axial with the rotor shaft, the z-axis pointing towards the bottom of OCT, and the y-axis obtained through the right-hand rule. The origin of ($\mathcal{T}_M$) is at the center of rotor rotation and does not rotate with the rotor, with the axial direction parallel to the x-axis, the tangential direction pointing toward the rotor's rotational direction, and the radial direction pointing outward from the rotor's center. Finally, ($\mathcal{T}_S$) is located at the center of the rotor's rotation and rotates with the rotor, and the ($\mathcal{T}_R$) frames are defined at the quarter chord line of each rotor blade section (VanZwieten et al., 2013).

The transformation matrix from ($\mathcal{T}_I$) to ($\mathcal{T}_B$) is defined by successive rotations about the yaw angle ψ, the pitch angle θ, and the roll angle ϕ (i.e., a 3-2-1 Euler angle sequence):

$$T_{\mathcal{T}_I}^{\mathcal{T}_B} = \begin{bmatrix} c_\psi c_\theta & s_\psi c_\theta & -s_\theta \\ c_\psi s_\theta s_\phi - s_\psi c_\phi & c_\psi c_\phi + s_\psi s_\theta s_\phi & c_\theta s_\phi \\ c_\psi s_\theta c_\phi + s_\psi s_\phi & -c_\psi s_\phi + s_\psi s_\theta c_\phi & c_\theta c_\phi \end{bmatrix} \tag{1}$$

where $s_{(.)} = \sin(.)$ and $c_{(.)} = \cos(.)$.

The 6 DOF kinematic equations are given (Fossen, 2011)

$$\begin{bmatrix} \dot{x} \\ \dot{y} \\ \dot{z} \\ \dot{\phi}_b \\ \dot{\theta} \\ \dot{\psi} \end{bmatrix} = \begin{bmatrix} uc_\psi c_\theta + v(c_\psi s_\theta s_\phi - s_\psi c_\phi) + w(s_\psi s_\phi + c_\psi c_\phi s_\theta) \\ us_\psi c_\theta + v(c_\psi c_\phi + s_\phi s_\theta s_\psi) + w(s_\theta s_\psi c_\phi - c_\psi s_\phi) \\ -us_\theta + vc_\theta s_\phi + wc_\theta c_\phi \\ p_b + qs_\phi \frac{s_\theta}{c_\theta} + rc_\phi \frac{s_\theta}{c_\theta} \\ qc_\phi - rs_\phi \\ q\frac{s_\phi}{c_\theta} + r\frac{c_\phi}{c_\theta} \end{bmatrix} \tag{2}$$

where $\theta \neq \pm 90°$, $(\bullet)$ denotes the time derivative, x, y, z are the Cartesian coordinates of the origin of the OCT main body ($\mathcal{T}_B$) with respect to the inertial reference frame, u, v, w are the linear velocities in the x, y, z directions respectively, $p_\bullet$ denotes the rotational velocities about the x-axis of ($\mathcal{T}_B$) with the subscript denoting a reference to either the main body, p_b, or the rotor p_r, q, r are the rotational velocities common to both the rotor and main body about y, z of ($\mathcal{T}_B$), respectively, ψ, θ, ϕ_b are the Euler angles describing the orientation of the OCT main body ($\mathcal{T}_B$) with respect to the inertial reference frame respectively.

2.1.2. Dynamic equations of motion

The dynamic equations of motion for the buoyancy-controlled OCT are described using 7-DOF: 6-DOF corresponding to the main rigid body which are based on Fossen (2011) with modifications to account for the rotation of the rotor as suggested in VanZwieten et al. (2013), and 1-DOF corresponding to the rotor's rotation about the x-axis of the ($\mathcal{T}_B$). These equations are obtained using the Newton–Euler approach, and they are summarized here from VanZwieten et al. (2013). Note that the following equation can be used to find the angular acceleration of the rotor directly using the system's states, inertial properties, electromagnetic torque, and hydrodynamic rotor torque

$$\dot{p}_r = \left[M_{x_r} - M_{x_s} - qr\left(I_{z_r}^v - I_{y_r}^v \right) \right] / I_{x_r}^v \tag{3}$$

where M_{x_s} denotes the electromagnetic shaft moment about the x-axis of ($\mathcal{T}_B$), M_{x_r} denotes the total external rotor moment about the x-axis of ($\mathcal{T}_B$), $I_{\bullet_r}^v$ denotes the virtual mass moment of inertia of the rotor for x, y, z axes according to the bullet subscript.

The other six equations are coupled and they provide the acceleration components.

$$\begin{bmatrix} \dot{u} & \dot{v} & \dot{w} & \dot{p}_b & \dot{q} & \dot{r} \end{bmatrix}^{\mathrm{T}} = M^{-1}C \tag{4}$$

where

$$M = \begin{bmatrix} m^v & 0 & 0 & 0 & m_b^v z_{G_b}^v & 0 \\ 0 & m^v & 0 & -m_b^v z_{G_b}^v & 0 & m^v x_G^v \\ 0 & 0 & m^v & 0 & -m^v x_G^v & 0 \\ 0 & -m_b^v z_{G_b}^v & 0 & I_{x_b}^v & 0 & -I_{xz_b}^v \\ m_b^v z_{G_b}^v & 0 & -m^v x_G^v & 0 & I_y^v & 0 \\ 0 & m^v x_G^v & 0 & -I_{xz_b}^v & 0 & I_z^v \end{bmatrix} \tag{5}$$

$$C = \begin{bmatrix} f_x + m^v(vr - wq) + m^v x^v_G \left(q^2 + r^2\right) - m^v_b z^v_{G_b} p_b r \\ f_y - m^v ur + w\left(m^v_b p_b + m^v_r p_r\right) - m^v_b z^v_{G_b} qr \\ -m^v_b x^v_{G_b} qp_b - m^v_r x^v_{G_r} qp_r \\ f_z + m^v uq - v\left(m^v_b p_b + m^v_r p_r\right) + m^v_b z^v_{G_b}\left(p_b^2 + q^2\right) \\ -m^v_b x^v_{G_b} rp_b - m^v_r x^v_{G_r} rp_r \\ M_{x_b} + M_{x_s} - qr\left(I^v_{z_b} - I^v_{y_b}\right) + I^v_{xz_b} p_b q \\ -m^v_b z^v_{G_b}\left(wp_b - ur\right) \\ M_y - rp_b\left(I^v_{x_b} - I^v_{z_b}\right) - rp_r\left(I^v_{x_r} - I^v_{z_r}\right) - I^v_{xz_b}\left(p_b^2 - r^2\right) \\ +m^v_b z^v_{G_b}(vr - wq) - m^v x^v_G uq + m^v_b x^v_{G_b} vp_b + m^v_r x^v_{G_r} vp_r \\ M_z - qp_b\left(I^v_{y_b} - I^v_{x_b}\right) - qp_r\left(I^v_{y_r} - I^v_{x_r}\right) - I^v_{xz_b} rq \\ -m^v x^v_G \text{ u } r + m^v_b x^v_{G_b} wp_b + m^v_r x^v_{G_r} wp_r \end{bmatrix} \tag{6}$$

where m is the mass of the entire OCT or the component denoted by a subscript, $(\bullet)^v$ denotes that the virtual mass, the virtual product of inertia, or virtual center of gravity, $(\bullet)_r$ denotes the rotor portion of the system (everything attached to the rotor and aft of the shaft), $(\bullet)_b$ denotes the main body portion of the system (everything that is not attached to the rotor and aft of the shaft), $(\bullet)_G$ denotes the center of gravity, $f_\bullet$ denotes the total external force in the direction of its subscript defined in $(\mathcal{T}_B)$, $M_\bullet$ denotes the total external moment about the axis denoted by its subscript defined in $(\mathcal{T}_B)$, $I_\bullet$ denotes the mass moment or product of inertia denoted by its subscript defined in $(\mathcal{T}_B)$, $[\bullet]^{-1}$ denotes the inverse operator.

In the dynamic equations of motions given in Eqs. (5)–(6), f_x, f_y, and f_z are the net external forces on the OCT system (the main body and rotor collectively) in the x, y, and z directions shown in Fig. 1, M_y and M_z are the net external moments on the ocean current turbine system (the main body and rotor collectively) about the y and z directions shown in Fig. 1. Additionally, M_{x_b} is the total external moment on the main body (i.e., everything that does not rotate with the rotor) of this OCT system and M_{x_r} is the total external moments on the rotor (and everything that rotates with the rotor) portion of this OCT system.

The OCT equations of motion, which include the kinematics in Eq. (2) and dynamics in Eqs. (3)–(4) represent a set of strongly coupled nonlinear first-order autonomous ODEs that can be written formally as

$$\dot{x}_p = f(x_p, u_p, \eta_c, \mathcal{V}_c, \mathbf{V}_w, C) \tag{7}$$

where x_p and u_p represent the state vector and control vector; $\eta_c = [x_c \ y_c \ z_c]^{\mathrm{T}}$ and $\mathcal{V}_c = [u_c \ v_c \ w_c]^{\mathrm{T}}$ denote the Cartesian coordinates and linear velocities of the mooring cable nodes respectively; $\mathbf{V}_w = [U_w \ V_w \ W_w]^{\mathrm{T}}$ denotes a vector of the ocean current velocity; $C = [C_A \ C_T]$ denotes a matrix of axial and tangential induction coefficients calculated over the swept area of the rotor blade, which are found using the angles of attack, lift coefficient, drag coefficient, and flow field (see VanZwieten et al., 2013 for details). The state vector, x_p, and the control vector, u_p, are defined as:

$$x_p = [u \ v \ w \ p_b \ p_r \ q \ r \ x \ y \ z \ \phi_b \ \phi_r \ \theta \ \psi]^{\mathrm{T}} \tag{8}$$

$$u_p = [B_f \ B_a]^{\mathrm{T}} \tag{9}$$

where the control input includes front and aft buoyancy chamber fill fractions, B_f and B_a, respectively.

2.2. Actuators - variable buoyancy system

The OCT system used in this work has one type of actuator defined as follows.

Variable Buoyancy System Model: The variable buoyancy system has two separate variable buoyancy chambers. Each chamber can hold 31.251 m^3 of air/water and is sufficiently baffled such that the center of mass of the ballast in each chamber does not depend on OCT orientation.

This model is developed to predict ballast pump power usage to provide reasonable limits on the rate at which water can be transferred into or out of these chambers.

The power required to pump seawater out of the buoyancy tank can be calculated using pressure, volumetric flow rate, Q_{B}, and pump efficiency, η_{pump}:

$$P_{\mathrm{B}}^{empty} = \frac{PQ_{\mathrm{B}}}{\eta_{\mathrm{pump}}} \tag{10}$$

where $\eta_{\mathrm{pump}} = 0.75$ is the pump efficiency, $P = P_{\mathrm{atm}} + P_{\mathrm{HS}}$. Assuming P_{atm} is atmospheric pressure (101 kPa) and P_{HS} is hydrostatic pressure (i.e. $P_{\mathrm{HS}} = \rho.g.z$) in kPa, where $g = 9.81$ m/s^2 is the gravitational acceleration. P_B^{empty} in kW can be rewritten as:

$$P_{\mathrm{B}}^{\mathrm{empty}} = \frac{(101 + 10.1z)Q_{\mathrm{B}}}{0.75} \tag{11}$$

To define the constraints on the slew rates, the limits for the volumetric flow rate of water as a function of depth should be calculated. This can be rewritten as:

$$Q_{\mathrm{B}} = \frac{0.75 P_{\mathrm{B}}^{\mathrm{empty}}}{101 + 10.1z} \tag{12}$$

At the typical operational point, a depth of 50 m, the volumetric flow rate, Q_{B}, is 0.023 m^3/s by assuming a ballast pump power equal to the WWII era submarines, i.e. $P_{\mathrm{B}}^{\mathrm{empty}} = 18.8$ kW (Navy, 2008). Since each of the two ballast chambers has a volume of 31.251 m^3, these chambers can be completely emptied in 22.2 min at this depth.

2.3. Faulty rotor models

In this section, the modeling details of the rotor faults are described. For energy production turbines, wind or ocean, rotor faults can occur as a result of manufacturing defects and construction, or they can occur during their service life because of the accumulation of wear and tear. The most common rotor faults can be categorized as a pitch offset (Freeman et al., 2019), hydrofoil performance degradation, or mass imbalance.

In this work, we focus on pitch offset faults occurring in one of the three blades of the OCT system described in the sections above. In Fig. 2, the healthy rotor blade 2(a), and faulty rotor blade 2(b) diagrams are shown. The pitch angle of one blade differs from the other blades' pitch angle, and so the balance in the hydrodynamic behaviors of the blades is disrupted during the operation. This disruption is caused due to having a different angle of attack in the faulty blade, which makes the axial and tangent hydrodynamic forces, F_a, F_t, diverge and result in unbalanced moments of inertia and torques onto the turbine's rotor shaft (Jiang et al., 2009).

For a blade pitch offset fault, the blade pitch angle of one blade, β_e, is offset from the other blade pitch angles by β_i:

$$\beta_e = \beta_{\mathrm{ref}} - \beta_i \tag{13}$$

where the desired pitch angle of all blades is β_{ref}.

In a healthy rotor blade, the blade pitch angle is equal to the desired one, and so $\beta_e = 0$. To simulate a blade pitch offset fault, a blade angle of β_e is used to replace the default angle of a single rotor blade in the nonlinear model given in 2.1, and then the linearize faulty models are obtained in the same manner as explained in the following section.

2.4. Linearization process

Several linear models are derived from the nonlinear model discussed in Section 2.1. These models are used later (i.e. in Section 4.3) for the multi-model approach to control design. All linear models of

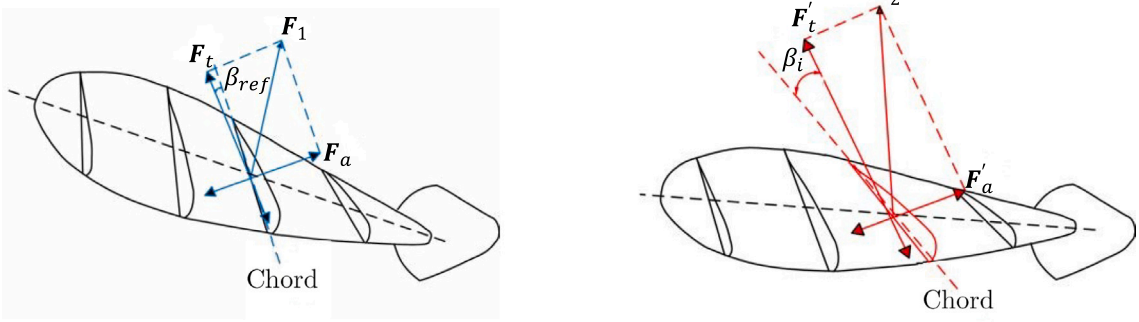

(a) Healthy rotor blade, where the blade pitch angle is aligned with its angle of attack.

(b) Faulty rotor blade, where the blade pitch angle is aligned with its angle of attack.

Fig. 2. The pitch offset faults representations (Freeman et al., 2019).

the faulty OCT used in this article are determined for the pitch fault conditions. The resulting linear systems are written as:

$$\delta\dot{x}_p = \begin{bmatrix} \delta\dot{u} \\ \delta\dot{v} \\ \delta\dot{w} \\ \delta\dot{p}_b \\ \delta\dot{q} \\ \delta\dot{r} \\ \delta\dot{x} \\ \delta\dot{y} \\ \delta\dot{z} \\ \delta\dot{\phi}_b \\ \delta\dot{\theta} \\ \delta\dot{\psi} \end{bmatrix} = [A_p] \begin{bmatrix} \delta u \\ \delta v \\ \delta w \\ \delta p_b \\ \delta q \\ \delta r \\ \delta x \\ \delta y \\ \delta z \\ \delta\phi_b \\ \delta\theta \\ \delta\psi \end{bmatrix} + [B_p] \begin{bmatrix} \delta B_f \\ \delta B_a \end{bmatrix} + [F_p] \begin{bmatrix} \delta U_N \\ \delta U_E \\ \delta U_D \end{bmatrix} \tag{14}$$

where δ denotes the difference between the state or control variables and the equilibrium values about which the system is linearized, A_p is the system matrix, and B_p is the input matrix. F_p is the flow matrix where $\delta U_{\bullet}$ denotes the differences in the flow speed for the North, East, and Down axes according to the bullet subscript.

The output vector, y_p, is defined as

$$\delta y_p = [C_p] \begin{bmatrix} \delta u & \delta v & \delta w & \delta p_b & \delta q & \delta r & \delta x & \delta y & \delta z & \delta\phi_b & \delta\theta & \delta\psi \end{bmatrix}^{\mathrm{T}} \tag{15}$$

where C_p is the output matrix, which is an identity matrix of 12×12.

This linearization is conducted for a steady and homogeneous flow field about the equilibrium states and control values. To remove the dependence of the linear system response on rotor blade rotation angle, ϕ_r, the system response is averaged over one rotor blade rotation when calculating equilibrium values. Additionally, this linear model assumes that the rotor is rotating at a constant rotational speed, $\dot{\phi}_r = constant$, thus reducing the number of states in the linear model to 12 (from 14 for the non-linear model).

The matrices of the linear model corresponding to the healthy case, i.e., system matrix A_p and input matrix B_p, are presented in the Appendix B. They were obtained using the following process that utilizes the described nonlinear model, as in Section 2.1. To remove the dependence of linear system models on the states of the individual cable nodes, all intermediate cable nodes were assumed to fall to unique equilibrium values based on the perturbations applied during each step of the linearization process. Quasi-static cable force dependencies on OCT position and attitude were determined by recalculating equilibrium cable node states and the resulting forces on the OCT during linearization each time the OCT position or attitude states were varied. Dependencies of cable forces on the OCT velocity states were accounted for during linearization by allowing velocity perturbations to alter cable node position and velocity equilibrium states. This allows the effects of changes in all OCT states to be incorporated into the linear model without directly accounting for the individual cable node states.

3. Multi-model predictive control design for fault-tolerant control

We propose a novel method based on multiple linear models and model predictive control, which is abbreviated as Multi-Model Predictive Control (MMPC). Because it uses multiple models for control design, this method is expected to handle nonlinearities much better than a method that uses a single linear model obtained via linearization around only one operating point. For the same reason, this method can improve robustness and thus have better performance when system failures occur than a control method that uses only one model. Also, this method will benefit from MPC advantages, such as the excellent capability of MPC to handle multiple states, outputs, and control inputs and to guarantee that numerous system constraints are not violated. The method is described in detail next and is illustrated on the control of OCT when failures occur.

3.1. Linearized system sets definition

For the MMPC method description, several linear systems and system sets must be defined as follows.

Consider the following set of continuous linear time-invariant (CLTI) systems:

$$\dot{x}_p = A_p x_p + B_p u_p \tag{16}$$

$$y_p = C_p x_p + D_p u_p \tag{17}$$

for $p = 1, 2, \ldots, N$. The corresponding set of discrete linear time-invariant (DLTI) systems is:

$$x_p(k+1) = A_{d_p} x_p(k) + B_{d_p} u_p(k) \tag{18}$$

$$y_p(k) = C_{d_p} x_p(k) + D_{d_p} u_p(k) \tag{19}$$

Each discrete linear time-invariant (DLTI) system is obtained via standard discretization of a CLTI, i.e., the discretized system matrices are

$$A_{d_p} = e^{AT_d}, \quad B_{d_p} = \int_{\tau=0}^{T_d} e^{A_p \tau} B_p d\tau, \quad C_{d_p} = C_p, \quad D_{d_p} = D_p. \tag{20}$$

The sampling time, T_d, used for discretization is determined according to the Shannon sampling theorem described in Jerri (1977) after determining the dominant eigenvalues as explained in Section 4.1.1 on the applied system.

The set of CLTI systems described by Eqs. (16)–(17) or in DLTI form by Eqs. (18)–(19) will be called the *model bank*. These systems represent

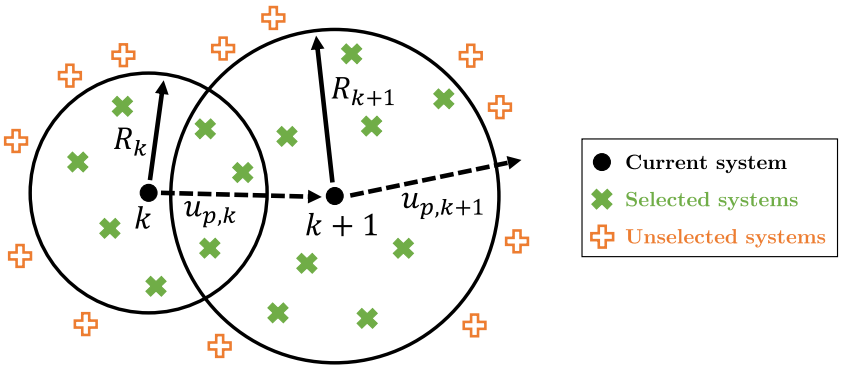

Fig. 3. Visualization of the selected models' selection process at time steps k and $k+1$.

all of the linear models used throughout the MMPC method application. In the specific case of MMPC for OCT with failures, they will include the *nominal linearized model* (i.e., corresponding to the ideal operating condition), as well as models of faulty OCT systems. The *model bank* is built offline before the system is launched, based on the expected states and conditions (e.g., failures) of the physical system (the OCT in this application). The state vector, x_p, and the control vector, u_p, are the same vectors as defined in Section 2.1.2 as Eq. (7).

The *current model* is the linear model obtained via linearization of a nonlinear model at the current time. Note that this model may or may not be part of the *model bank* because the *model bank* is built before the system is launched. The current OCT state and condition (e.g., faulty OCT or healthy) may or may not be among the ones used when the *model bank* was created.

The *selected models* set is a subset of the *model bank* which, at the current time, contains elements of the *model bank* that are "close enough" (in a sense that will be made mathematically precise shortly) to the current model. The *selected models* set is dynamically evolving in time: some elements of the *model bank* may enter this set while others may leave as time progresses.

To understand the process of determining the *selected models* and the manner in which the individual control actions are combined, a brief review of the ν-gap, a robust control metric that has proven very effective (Vinnicombe, 1993), is necessary and is given next.

3.2. The ν-gap metric

There are several metrics that capture the closeness between plants, and the ν-gap metric, i.e. Vinnicombe gap, was introduced in Vinnicombe (1993) and was proved to be less conservative than its precursor, the gap metric (El-Sakkary, 1985). The ν-gap metric measures the closeness between two plants based on their closed-loop behavior, and its numerical value is between 0 and 1. If the plants have similar closed-loop behavior, the value is closer to zero, and if they have different closed-loop characteristics, the value is 1. The ν-gap metric is very useful in robust control design: if P_1 and P_2 are two LTI models of a physical system, and if the ν-gap is sufficiently small, then any feedback controller which is satisfactory for one model will also be satisfactory for the other. Thus, the difference between P_1 and P_2 is not important from a feedback control perspective. The numerical value of ν-gap metric is used in Eq. (36) to obtain the aggregated control input from multiple plants, which is explained in Section 3.4.2.

The ν-gap metric, $\delta_\nu(\cdot,\cdot)$, was defined mathematically in Vinnicombe (1993) as:

$$\delta_\nu(P_1,P_2) := \begin{cases} \|\tilde{G}_2 G_1\|_\infty & \text{if } det(G_2^* G_1)(j\omega) \neq 0 \ \forall\omega \text{ and wno } det(G_2^* G_1) = 0 \\ 1 & \text{otherwise} \end{cases} \tag{21}$$

where:

$$G_i := \begin{bmatrix} N_i \\ M_i \end{bmatrix}, \tag{22}$$

$$\tilde{G}_i := \begin{bmatrix} -\tilde{M}_i & \tilde{N}_i \end{bmatrix}, \tag{23}$$

$$\|G\|_\infty = sup \left\{ \frac{\|G\hat{v}\|_2}{\|\hat{v}\|_2} : \hat{v} \neq 0 \right\}, \tag{24}$$

P_1 and P_2 are two continuous LTI systems that we want to compute the ν-gap between, wno(r) is the winding number around the origin of $r(s)$ when s follows the Nyquist D-contour, $\cdot^*$ is the complex conjugate transpose, and $[N_i, M_i]$ and $[\tilde{M}_i, \tilde{N}_i]$ denote a normalized right and left coprime factorization of P_i respectively. For practical applications, including the results in this article, the "nugap" function from MATLAB's μ-Analysis and Synthesis Toolbox is used to calculate the ν-gap (the details of the computational method are given in Vinnicombe, 1999).

3.3. Construction of the selected models set

To construct the *selected models* set from the *model bank*, the following process is applied. At each discrete time step, k, determined by the MPC implementation, the ν-gap between the *current model* and each exponentially stable element of the *model bank* is calculated. If this ν-gap is smaller than a prescribed value (i.e. ν-gap radius), R_k, the corresponding system from the *model bank* is included in the *selected models* set.

In other words, a sphere centered at the *current model* and with radius (as defined by the ν-gap metric) equal to R_k is created, and the exponentially stable systems from the *model bank* which are interior to this sphere are included in it. At the next time step, $k+1$, the process is repeated: the *current model* at time step $k+1$ is considered to create a new sphere of radius R_{k+1} and the exponentially stable systems from the *model bank* which belong to the interior of this sphere are selected to construct the *selected models* set at time step $k+1$.

The generalized concept of the process is schematically represented in Fig. 3, each DLTI system inside the *model bank* is represented as "**x**", and *selected models* at each time step k are the ones inside the circle defined by the ν-gap radius R_k. The selected models are represented with green color at each time step k, and the ones left out of the ν-gap radius R_k are shown with orange color. Also, a summary of the selection algorithm is given in Algorithm 1.

In Section 4, the application of the process on OCT is given in detail. In the OCT application, the *current model* and the ν-gap radius are chosen to be the same through the designated operation duration, and it is assumed that the information about the degree of fault in the system has already been detected by a separate algorithm as given in Freeman et al. (2021, 2022), which is out of scope of this work.

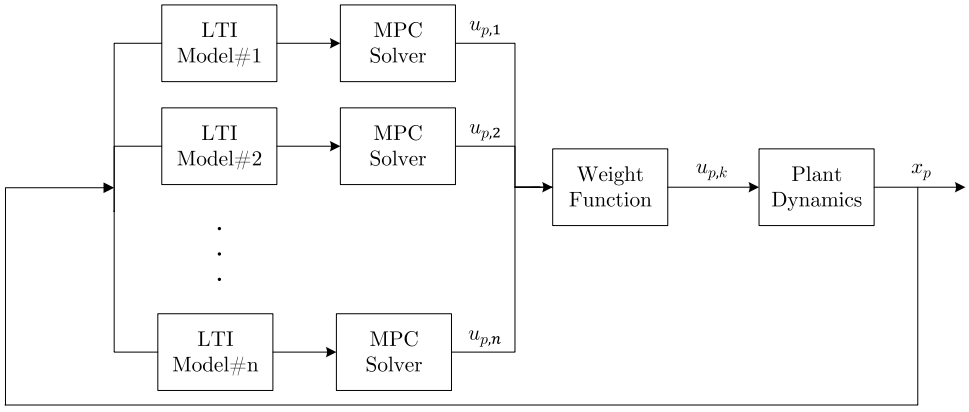

Fig. 4. Multi-model predictive control architecture.

Algorithm 1 Construction the selected models set

1: Create the *model bank*
2: Define the *selected models* to be used in MMPC according to R_k;
3: **for** $k = 1$ *to* $N_{\text{operation length}}$ **do**
4: The ν-gap between the *current model* and *model bank* is calculated.
5: **if** ν-gap $< R_k$ **then**
6: The corresponding system is included in the *selected models* set.
7: **end if**
8: **end for**

3.4. Aggregate control action for the MMPC algorithm

At the current time, for each system in the *selected models* set, MPC design generates a discrete sequence of control actions. These are combined to generate an "aggregate" control action, $u_{p,k}$, which is applied to the linear or nonlinear *current model* at step time k, depending on the model that is available or feasible. Of course, in a practical implementation, this control action will be applied to the physical system and not to a model of the system; however, in design studies (like this one), it is applied to a model. This control architecture is represented in Fig. 4 and related details are discussed next.

3.4.1. MPC cost function

To design an MPC for a generic DLTI system indexed by p as given in Eqs. (16)–(17), the following cost must be minimized subject to constraints:

$$\begin{aligned}\tilde{V}(k) \equiv \frac{1}{2}\Bigg(&\sum_{i=k+1}^{k+H_p-1}\left(\left(y_{i|k}-r_i\right)^T Q_{part}\left(y_{i|k}-r_i\right)\right)\\ &+\sum_{i=k}^{k+H_c-1}\Big(\left(u_{i|k}-u_{i-1|k}\right)^T R_{\Delta\text{part}}\left(u_{i|k}-u_{i-1|k}\right)\\ &+\left(u_{i|k}-d_i\right)^T R_{\text{part}}\left(u_{i|k}-d_i\right)\Big)\\ &+\left(y_{k+H_p|k}-r_{k+H_p}\right)^T Q_{\text{term}}\left(y_{k+H_p|k}-r_{k+H_p}\right)\Bigg)\end{aligned} \tag{25}$$

where k is the current time index, H_p is the prediction horizon, H_c is the control horizon, $y_{i|k}$ is the vector of the outputs at time step i, r_i is the vector of the target outputs at time step i, $u_{i|k}$ is the vector of the control inputs at time step i, d_i is the vector of the arbitrary user-selected target controls at time step i, Q_{part} is the user-selected weight matrix for the target outputs, Q_{term} is the user-selected weight matrix for the final target output, $R_{\Delta\text{part}}$ is the user-selected weight matrix for the control input changes, R_{part} is the user-selected weight matrix for the desired control inputs.

Quadratic form of the cost function

After algebraic manipulations as described in Greer and Sultan (2020), the cost function is converted to a quadratic form as follows:

$$\tilde{V}(k) = \frac{1}{2}u_{k|k,H_c}^T S u_{k|k,H_c} + f^T u_{k|k,H_c} + c \tag{26}$$

where

$$S = H^T Q_{\text{tot}} H + G^T R_\Delta G + R_{\text{tot}} \tag{27}$$

$$c = \frac{1}{2}\left(F^T Q_{\text{tot}} F - 2F^T Q_{\text{tot}} r + r^T Q_{\text{tot}} r + J^T R_\Delta J + d^T R_{\text{tot}} d\right) \tag{28}$$

and

$$f = \left(H^T Q_{\text{tot}} F - H^T Q_{\text{tot}} r - G^T R_\Delta J - R_{\text{tot}} d\right) \tag{29}$$

The user-selected weight matrices are constructed as follows:

$$Q_{\text{tot}} = \begin{bmatrix} Q_{\text{part}} & \cdots & 0 & 0 \\ \vdots & \ddots & \vdots & \vdots \\ 0 & \cdots & Q_{\text{part}} & 0 \\ 0 & \cdots & 0 & Q_{\text{term}} \end{bmatrix} \tag{30}$$

where there is a number of H_p matrices along the diagonal of Q_{tot} and all other entries in the matrix are zeros.

$$R_\Delta = \begin{bmatrix} R_{\Delta\text{part}} & \cdots & 0 \\ \vdots & \ddots & \vdots \\ 0 & \cdots & R_{\Delta\text{part}} \end{bmatrix} \tag{31}$$

where there is a number of H_c number of $R_{\Delta\text{part}}$ matrices along the diagonal of R_Δ and the other entries in the matrix are zero.

Matrix R_{tot} follows the same structure as R_Δ, and it has H_c matrices R_{part} along the diagonal and the rest of the entries are zero:

$$R_{\text{tot}} = \begin{bmatrix} R_{\text{part}} & \cdots & 0 \\ \vdots & \ddots & \vdots \\ 0 & \cdots & R_{\text{part}} \end{bmatrix} \tag{32}$$

The constraints are written as follows:

$$u_j^{\min}(i) \le u_j(i) \le u_j^{\max}(i), \qquad i = 1, 2, \ldots, m \tag{33}$$

$$\Delta u_j^{\min}(i) \le \Delta u_j(i) \le \Delta u_j^{\max}(i), \qquad i = 1, 2, \ldots, m \tag{34}$$

$$y_{g+1}^{\min}(i) \le y_{g+1}(i) \le y_{g+1}^{\max}(i), \qquad i = 1, 2, \ldots, h \tag{35}$$

for all integers j such that $k \le j \le k + H_c - 1$ and all integers g such that $k \le g \le k + H_p - 1$, where m is the number of controls, h is the number of outputs, $a_j(i)$ is the i value of a at time step j (a can be u, Δu or y),

$a_j^{\min}(i)$ and $a_j^{\max}(i)$ are the minimum and maximum values respectively of $a_j(i)$, Δu is the control change at time step j is the difference between the previous control and the new control at time step j.

The cost function given in Eq. (26) is strictly convex if S in Eq. (27) is positive definite. With constraints, the MPC design problem is converted into a quadratically constrained optimization problem, where the quadratic cost, Eq. (26), is minimized subject to inequality constraints as listed in Eqs. (33)–(35). This formulation of the optimization problem is solved efficiently using interior point methods (Vanderbei and Carpenter, 1993; Altman and Gondzio, 1999).

3.4.2. Weight function & aggregate control input

Recall that if P_1 and P_2 are LTI models of a physical system, and the ν-gap between P_1 and P_2 is small, then the difference between P_1 and P_2 is not important from a feedback control perspective. This justifies the following definition. The similarity factors $\gamma_i(t)$ for the systems in the *selected models* set at a given discrete time step k (i.e. at time t_k) are

$$\gamma_i(t_k) = \delta_\nu(F_i, F), i = 1, \dots, N_m \tag{36}$$

where F_i are the *selected models* models, F is the *current model*, and N_m is the number of *selected models*. These factors are used to define the combination weights $w_i(t_k)$ at a given discrete time instant t_k as:

$$w_i(t_k) = \frac{(1-\gamma_i(t_k))^{ke}}{\sum_{j=1}^{N_m}(1-\gamma_j(t_k))^{ke}}, i = 1, \dots, N_m \tag{37}$$

where ke is a tuning factor.

Note that a small $\gamma_i(t_k)$ means that the *current model* has a response closer to that of P_i, so $w_i(t_k)$ has a larger value. Therefore, the controller developed using the P_i model has a bigger weight and is more important in the global control action.

The resulting aggregate control input $u_p(t_k)$ is:

$$u_p(t_k) = \sum_{i=1}^{N_m} w_i(t_k) u_i(t_k) \tag{38}$$

where $u_i(t_k)$ is the current control action generated by the MPC algorithm used on the *selected models* set F_i. The aggregate control is implemented on the *current model* to obtain the next system state. Then, the selected model set is updated as described previously, and the process is repeated until the terminal point is reached.

3.5. Algorithm steps

In this section, the algorithm steps of the MMPC are given as a summary of the previous sections, divided into offline and online parts.

Offline Steps

1. Obtain the CLTI system models set Eqs. (16)–(17) from the high-fidelity nonlinear model for various pitch blade faults by linearizing it around the equilibrium conditions given in Tables 6 and 7.
2. Conduct stability analysis to find the eigenvalue which determines the sampling time, T_d, satisfying the minimum requirement based on the Shannon sampling theorem.
3. Based on the stability analysis, eliminate the unstable systems inside the CLTI set to obtain the *model bank*.
4. Using the "nugap" function in MATLAB, construct the ν-gap table for the *selected models* with the values of Eq. (36) as given in Table 2.
5. Discretize the CLTI models Eqs. (16)–(17) obtained in Step 1 to generate DLTI systems Eqs. (18)–(19).
6. Define the actuator constraints and slew rate constraints of the system.
7. Define the prediction and control horizon, H_p, H_c,
8. Define the following properties for the cost function $\tilde{V}$ in Eq. (25):
   - Reference vector, r, which includes the optimal path to generate maximum power,
   - User-selected weight matrices, Q_{part}, Q_{term}, $R_{\delta\text{part}}$, R_{part},

Online Steps

The online steps of the MMPC are given in Algorithm 2 below. Since there are several loops inside, a listing structure is preferred to represent the online part of the MMPC used in this article.

Algorithm 2 Multi-model predictive control

```
Identify the pitch blade fault angle in the system;
Define the ν-gap radius, R_k, and the tuning factor ke in Eq. (37);
Define the selected models to be used in MMPC according to R_k;
for i = 1 to N_operation length do
    for j = 1 to N_selected models do
        Define the DLTI plant j to be used in MPC;
        Using the interior point method, solve the cost function Ṽ in Eq. (25);
        Obtain optimal [u_j*(i|H_c), ..., u_j*(i|i+H_c−1)] and save its initial input u_j*(i|H_c);
    end for
    Using the weight function given in Eq. (37), obtain the aggregate control input u_p*(i|H_c) from u_j*(i|H_c) vectors;
    Apply u_p*(i|H_c) to the faulty DLTI plant and obtain the next system state x(i + 1);
end for
```

4. Multi-model predictive control of MIMO nonlinear systems with actuator failures case study: Ocean current turbine system

4.1. Linearized models analysis

The nonlinear OCT model is linearized around a nominal condition that corresponds to maximum power production in steady axial flow. This condition is characterized by averaged flow velocity of 1.6 m/s and the following equilibrium control values,

$$u_{p_{eq}} = \begin{bmatrix} 46.77\% & 46.77\% \end{bmatrix}^{\mathrm{T}}, \tag{39}$$

and the following equilibrium state values were obtained for the healthy case:

$$x_{p_{eq}} = \begin{bmatrix} 0 & 0 & 0 & 0 & 0 & 0 & 554.50\ \text{m} & 0.38\ \text{m} & 50.00\ \text{m} & 0.01^\circ & 0 & 3.14^\circ \end{bmatrix}^{\mathrm{T}} \tag{40}$$

These equilibrium values for the control inputs and the states both change when the OCT system experiences failures (i.e. faulty conditions). Their values are tabulated in Table 6 for the equilibrium states, $x_{p_{eq}}$, and in Table 7 for the equilibrium control inputs, $u_{p_{eq}}$ as given in Appendix B. When finding these equilibrium conditions, the control variables are manipulated until the operating depth is approximate $z_{eq} = 50m$ (within ±8 cm) and pitch, θ_{eq}, is nearly zero (within ±0.015 degrees) to maximize power production and achieve the targeted depth. For this reason, the equilibrium states are very similar for all faults, while the corresponding equilibrium control varies significantly.

4.1.1. Stability analysis — eigenvalue–eigenvector analysis

Eigenvalue–eigenvector analysis is performed using the nominal healthy linear system to identify the dominant dynamics. This study is also necessary to choose the sampling time for system discretization. For the linearized system of the healthy OCT, i.e., described by (B.1)

Table 1
Eigenvector analysis of the linear OCT model.

Eigenmodes		$-0.1128 \pm 0.1645i$		$-0.0037 \pm 0.0024i$		
Index	State	Magnitude	Phase (°)	Magnitude	Phase (°)	
1	u	1.34×10^{-1}	∓55.60	1.02×10^{-3}	∓75.35	
2	v	9.20×10^{-2}	±174.68	4.16×10^{-3}	±147.68	
3	w	1.05×10^{-1}	∓88.53	1.08×10^{-3}	±104.55	
4	p_b	4.45×10^{-3}	±151.29	6.50×10^{-7}	±77.26	
5	q_b	6.22×10^{-4}	∓157.13	2.39×10^{-6}	±112.00	
6	r_b	2.56×10^{-2}	±172.70	6.98×10^{-6}	∓9.42	
7	x	6.74×10^{-1}	0	2.32×10^{-1}	∓42.92	Dominant States
8	y	4.61×10^{-1}	∓130.43	9.39×10^{-1}	±180	
9	z	5.27×10^{-1}	±146.42	2.54×10^{-1}	∓41.52	
10	ϕ_b	2.24×10^{-2}	±26.90	1.47×10^{-4}	∓70.78	
11	θ	1.95×10^{-3}	±101.90	5.51×10^{-4}	∓34.12	
12	ψ	1.28×10^{-1}	±48.27	1.58×10^{-3}	∓157.03	

Table 2
ν-gap metric table.

Fault	0°	1°	2°	3°	4°	5°	6°	7°	8°	9°	10°	12°	14°	16°	18°	20°
0°	0.00	0.41	0.40	0.40	0.50	1.00	0.96	0.62	1.00	0.95	1.00	1.00	1.00	1.00	0.48	0.71
1°	0.41	0.00	0.06	0.22	0.57	0.99	0.92	0.70	1.00	0.91	0.99	1.00	0.99	0.99	0.45	0.76
2°	0.40	0.06	0.00	0.28	0.62	0.98	0.89	0.74	1.00	0.88	0.98	1.00	0.97	0.98	0.43	0.79
3°	0.40	0.22	0.28	0.00	0.37	1.00	0.98	0.53	1.00	0.98	1.00	1.00	1.00	1.00	0.42	0.65
4°	0.50	0.57	0.62	0.37	0.00	1.00	1.00	0.20	1.00	1.00	1.00	1.00	1.00	1.00	0.41	0.47
5°	1.00	0.99	0.98	1.00	1.00	0.00	0.26	1.00	0.21	0.28	0.14	0.30	0.28	0.32	1.00	1.00
6°	0.96	0.92	0.89	0.98	1.00	0.26	0.00	1.00	0.44	0.09	0.32	0.50	0.33	0.40	0.98	1.00
7°	0.62	0.70	0.74	0.53	0.20	1.00	1.00	0.00	1.00	1.00	1.00	1.00	1.00	1.00	0.54	0.42
8°	1.00	1.00	1.00	1.00	1.00	0.21	0.44	1.00	0.00	0.45	0.14	0.13	0.20	0.25	1.00	1.00
9°	0.95	0.91	0.88	0.98	1.00	0.28	0.09	1.00	0.45	0.00	0.33	0.51	0.33	0.40	0.97	1.00
10°	1.00	0.99	0.98	1.00	1.00	0.14	0.32	1.00	0.14	0.33	0.00	0.22	0.14	0.19	1.00	1.00
12°	1.00	1.00	1.00	1.00	1.00	0.30	0.50	1.00	0.13	0.51	0.22	0.00	0.21	0.16	1.00	1.00
14°	1.00	0.99	0.97	1.00	1.00	0.28	0.33	1.00	0.20	0.33	0.14	0.21	0.00	0.08	1.00	1.00
16°	1.00	0.99	0.98	1.00	1.00	0.32	0.40	1.00	0.25	0.40	0.19	0.16	0.08	0.00	1.00	1.00
18°	0.48	0.45	0.43	0.42	0.41	1.00	0.98	0.54	1.00	0.97	1.00	1.00	1.00	1.00	0.00	0.58
20°	0.71	0.76	0.79	0.65	0.47	1.00	1.00	0.42	1.00	1.00	1.00	1.00	1.00	1.00	0.58	0.00

in Box I, (B.3), the eigenvalues are:

$$\begin{aligned} \lambda_{1,2} &= -0.2729 \pm 1.2585i, \quad & \lambda_{7,8} &= -0.1560 \pm 0.0661i, \\ \lambda_{3,4} &= -0.2563 \pm 0.9573i, \quad & \lambda_{9,10} &= -0.1128 \pm 0.1645i, \\ \lambda_{5,6} &= -0.1803 \pm 0.3755i, \quad & \lambda_{11,12} &= -0.0037 \pm 0.0024i \end{aligned} \tag{41}$$

As shown in Table 1, for the modes associated with the less damped eigenvalues (i.e., eigenvalues that are very close to the imaginary axis), the position states, x, y, z, are dominant (the associated magnitudes are the largest). Considering the OCT's working environment and its aim to maximize the energy harvested, the Z-position is the most important one considering the power density distribution (Haas, 2013; Lund et al., 2006). This is true because open ocean current speed typically varies much more rapidly in the vertical (z) direction than in the cross-stream (y) direction or in the downstream direction (x). The eigenvalue–eigenvector analysis shows that for the modes corresponding to the lightly damped eigenvalues ($-0.1128 \pm 0.1645i$ and $-0.0037 \pm 0.0024i$), the OCT coordinates are the dominant states. Thus, perturbations in the OCT position will be eliminated in a very long time, i.e., the OCT will return to the unperturbed nominal operating condition very slowly. This is not acceptable because the OCT must return to its unperturbed nominal operating condition in a very short time to avoid interference with shipping traffic or neighboring OCTs when deployed in arrays. OCT feedback control using MMPC can guarantee disturbance rejection and rapid return to the nominal unperturbed OCT state, as illustrated next.

This stability analysis is limited to be valid only for the linear models obtained around the equilibrium condition and for the environmental conditions of the ocean specified before. It is verified that the proposed control framework can successfully drive the OCT system between ± 20 m in depth, for a given flow speed of 1.6 m/s. These are the limitations of the OCT system application given here as an example. Therefore, if these conditions are modified (for example the system must operate in other locations of the ocean), the model bank should be extended to include models that correspond to these modified conditions. Extension of the model bank for additional equilibrium conditions requires additional numerical calculations, but as mentioned earlier these models are created offline. During the real-time operation, the algorithm only decides which models inside the model bank to be used and so model bank extension would not cause any burden on the computational performance online.

4.2. Multi-model predictive controller design

Following the discussion in Section 3, the weight matrices were selected for controller implementation as follows.

- Since it is desired to accurately track the depth reference, and the corresponding weight for the related state, z, indexed as 9 th in Q_{part} is set equal to 10. The system should be reaching that depth without violating the pitch limitation, and therefore the pitch angle state, θ indexed as 11 th in Q_{part} is set equal to 1, and the others equal to 0:

$$Q_{\text{part}} = \text{diag}\begin{bmatrix} 0 & 0 & 0 & 0 & 0 & 0 & 0 & 0 & 10 & 0 & 1 & 0 \end{bmatrix},$$

- To achieve or get closer to the reference points at the end of each prediction horizon, the weight matrix for the final (e.g., terminal) target output is chosen as 1:

$$Q_{\text{term}} = I_{12},$$

- To achieve the minimum control input change as the optimal solution calculated, the weight matrix for the desired control

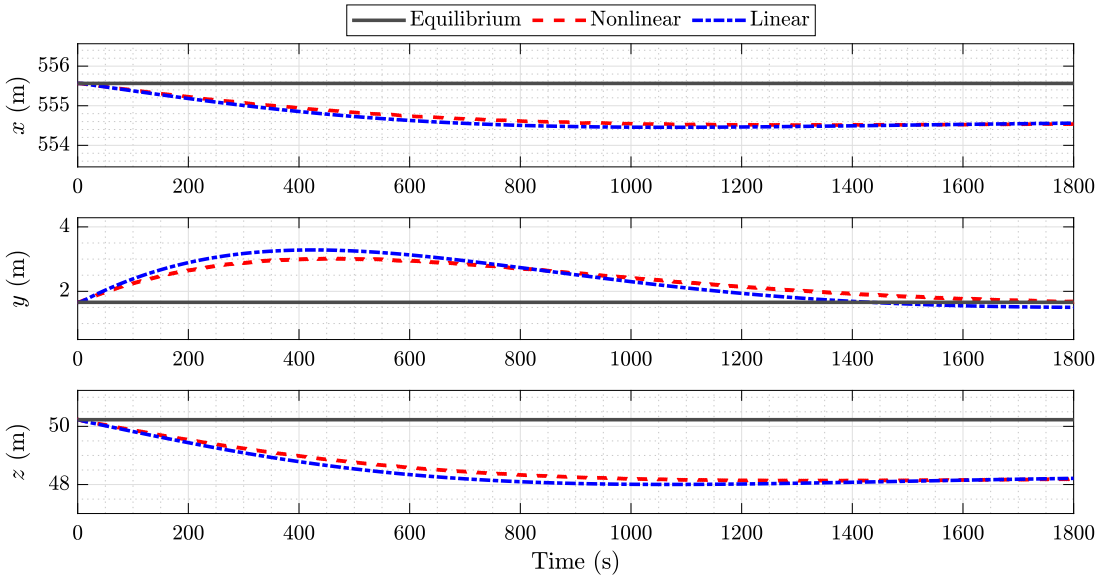

Fig. 5. Nonlinear vs linear simulations for +1% step change in B_f.

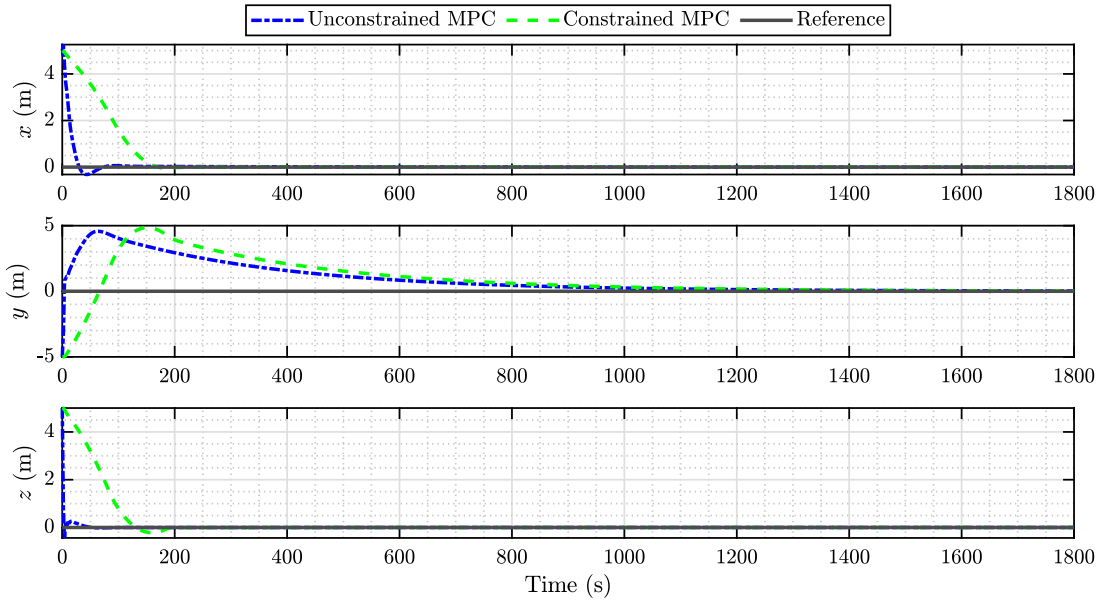

Fig. 6. Position states of the OCT system, comparison between the Unconstrained and Constrained MPC.

input changes is chosen as 1:

$$R_{\Delta\text{part}} = I_2$$

- The weight matrix for the desired control inputs is chosen as zero, as it satisfies the positive semi-definite requirement for the cost function, and the only requirement for the control input is to keep it as small as possible:

$$R_{\text{part}} = 0$$

where I_n is the $n \times n$ identity matrix.

Besides the user-selected matrices, the prediction horizon H_p and the control horizon H_c must be defined. For the OCT system, they were chosen as $H_p = 40$ to capture the important behavior of the OCT, and $H_c = 2$, to reduce the computation time per iteration. During tuning, it was observed that for a slow system like OCT, a longer prediction horizon does not improve the performance, but it only slows down the computation. Initially, the control horizon was given a high value, $H_c = 20$ which was half of the prediction horizon H_p, to avoid having problems during some extreme conditions (e.g., a higher degree of fault and higher change in the reference). In these cases, the optimization problem may become infeasible for short instances with the given actuator constraints, and the simulation was able to make use of the control inputs generated in the previous iteration for the horizon of 20. Several simulations for different faulty conditions were run for a much smaller control horizon ($H_c = 2$) in non-extreme conditions and any significant changes were not ascertained in the simulation results compared to when the control horizon was 20. Reducing the control horizon from 20 to 2, the computation time was decreased approximately by 13% per iteration. Since these horizons affect the computational time excessively for systems with multiple inputs like

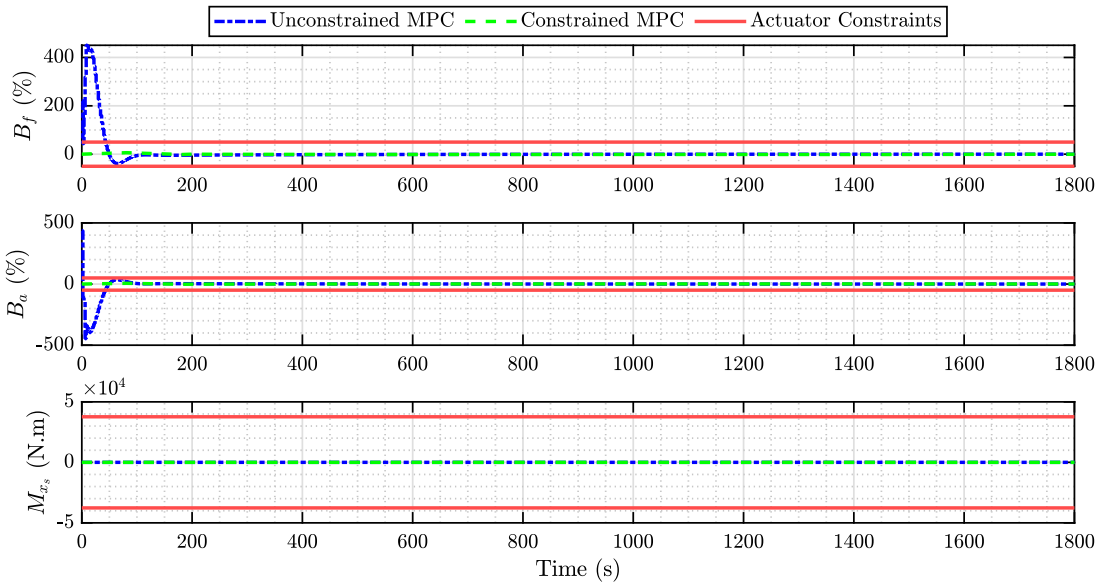

Fig. 7. Control inputs of the OCT system, comparison between the Unconstrained and Constrained MPC.

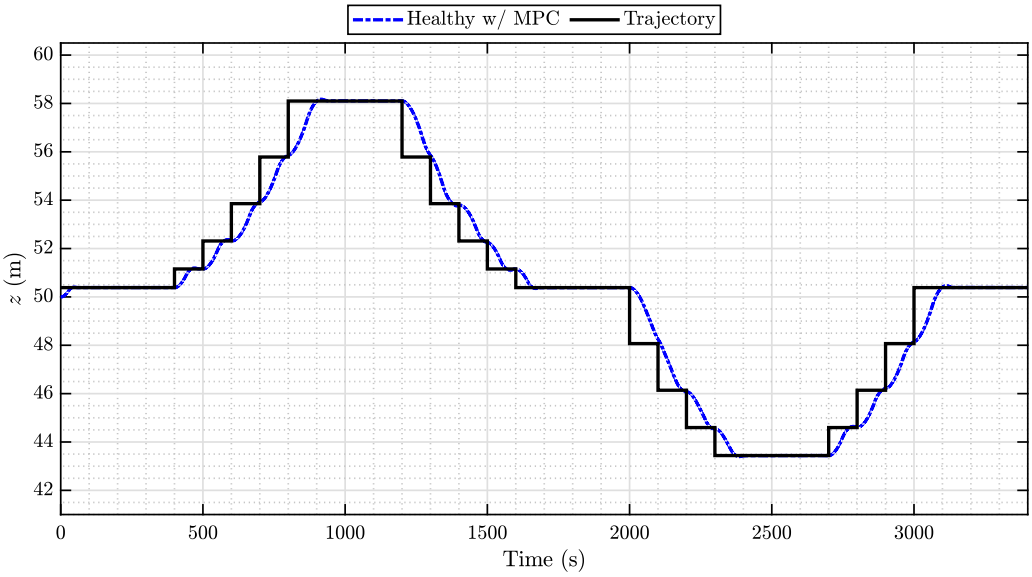

Fig. 8. The depth, z state, of the OCT as it follows the optimal trajectory.

OCTs, they were chosen as the minimum required values that capture with sufficient accuracy the dynamics of the system. Since the MPC's horizon is receding, the controller keeps calculating the next horizon values at every other time step. Therefore, avoiding the unnecessary future states' prediction is beneficial to reduce the computational cost while not compromising performance.

After defining the above elements related to the cost function, the system constraints must be specified to ensure that the optimal control inputs, i.e., the solution for the constrained optimization problem defined by MPC, is in the suitable range of the physical system. For OCT, the following were chosen:

$$\begin{bmatrix} |B_{\mathrm{a}}| & |B_{\mathrm{f}}| \end{bmatrix} \leq \begin{bmatrix} 50\% & 50\% \end{bmatrix} \tag{42}$$

and the slew rates constraints,

$$\begin{bmatrix} |\dot{B}_{\mathrm{a}}| & |\dot{B}_{\mathrm{f}}| \end{bmatrix} \leq \begin{bmatrix} 7.45\times10^{-6}\ \%/\mathrm{s} & 7.45\times10^{-6}\ \%/\mathrm{s} \end{bmatrix} \tag{43}$$

These constraints are defined by the physical model as given in Navy (2008) for the variable buoyancy actuator and in VanZwieten et al. (2013) for the generator. The MPC algorithm finds the control input actions based on these constraints so that the nonlinear system is controlled such that the real-life scenarios are simulated accurately.

4.3. Constructed model bank: ν-gap metric table of the faulty models

Following the procedure described in Section 2.3, 16 linear models of the OCT system were obtained. They constitute the *model bank* and the ν-gap values between them, computed as described in 3.2, and are tabulated in Table 2. In Table 2, "Fault" means the blade pitch offset fault, β_e as given in Eq. (13). Each column represents the ν-gap value between the model corresponding to the fault value written at the top of that column and the other models. For example, the first column gives the ν-gap values between the healthy model (for which $\beta_e = 0°$) and the other models. The diagonal of the table consists of zeros because the ν-gap value between a model and itself is 0.

From this *model bank*, the exponentially unstable ones, i.e., having at least one eigenvalue with a positive real part, are eliminated. The

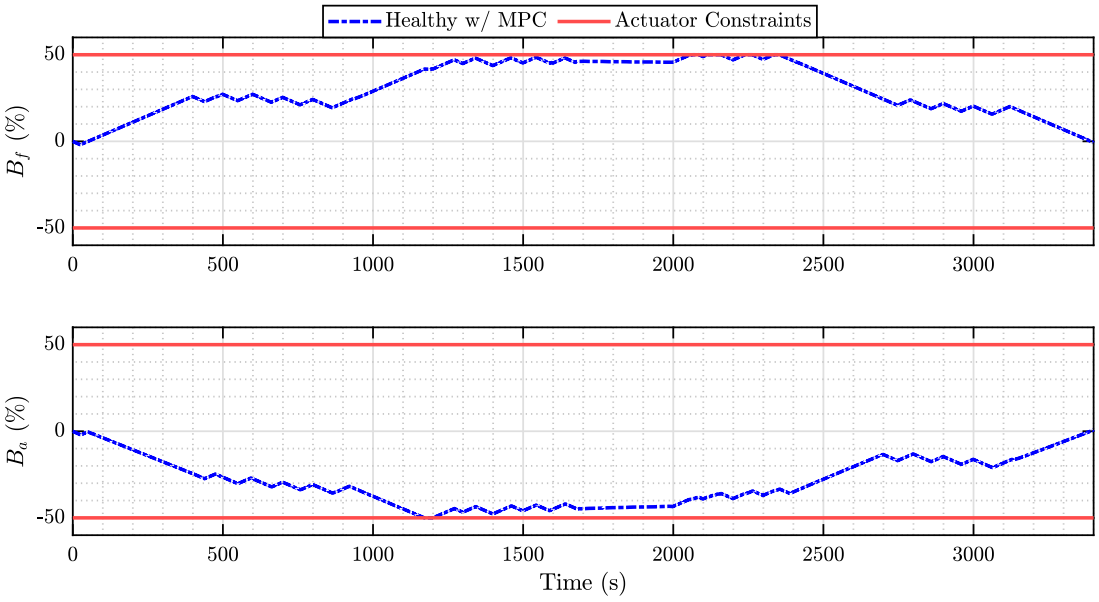

Fig. 9. Control inputs applied to the OCT system to track the optimal trajectory.

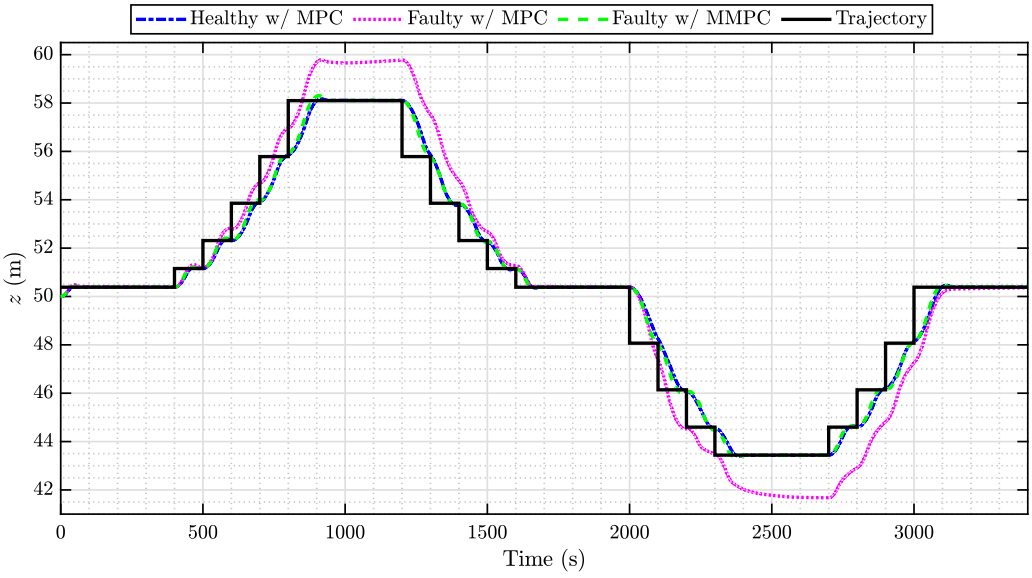

Fig. 10. The depth, z state, of the faulty & the healthy OCT systems during the optimal trajectory following.

models which survive this elimination process constitute the *selected models* set, and in the model bank given in Table 2, all of them are exponentially stable, and they will be used inside the MMPC without any elimination.

4.4. Simulation results

In this subsection, several simulation results are given to highlight the benefits of using MMPC for reference tracking (eventually, maximizing the power generation by going to the depth where the highest ocean current occurs) when there exists a blade pitch fault in the rotor.

4.4.1. Open-loop linear vs nonlinear systems comparison

The linearization process is verified by comparing the responses of the nonlinear system with those of the system linearized around the nominal equilibrium solution as given in Tables 6 and 7 in Appendix B.4. In the results provided in this section, both the healthy and the faulty systems are considered, and only one example is shown in Fig. 5, which belongs to the faulty system with $\beta_e = 1°$. Both systems are subjected to an identical step input change in the fill fraction of the front buoyancy chamber, B_f equal to +1%. The results for the position states variations, which are the most important, are shown in Fig. 5. It is ascertained that the linear model's responses follow a similar pattern to the nonlinear model's ones.

It must also be emphasized that, in the case of MPC, an agreement between linear and nonlinear responses is important only for the first seconds after the application of the step input or an external perturbation. This is true because of the nature of MPC, which repeatedly recomputes control actions every T_s second, i.e., 2 s for the OCT system,

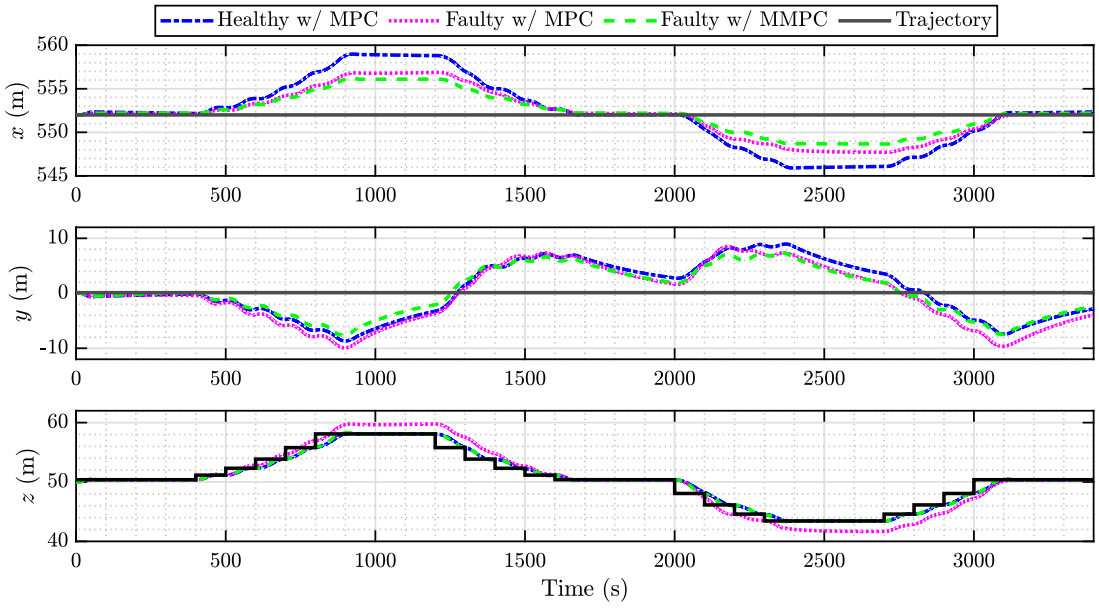

Fig. 11. Position states of the faulty & healthy OCT systems during the optimal trajectory following.

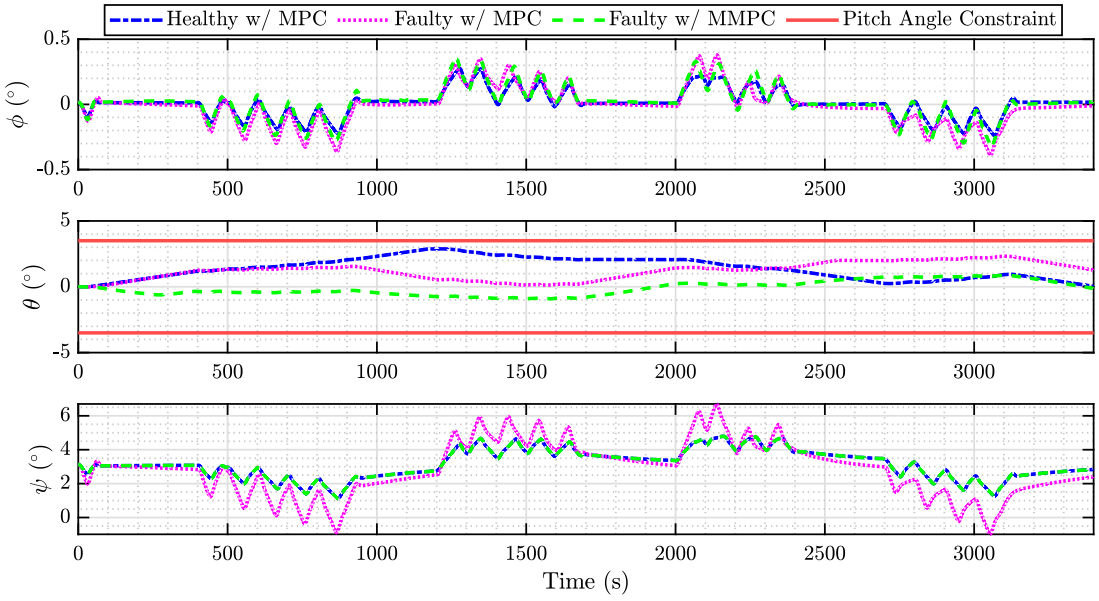

Fig. 12. Euler angles states of the faulty & healthy OCT systems during the optimal trajectory following.

and takes the current state of the system into account during that computation.

We also remark that the behavior of the position states is representative of the variation of other states, i.e., small discrepancies between the nonlinear and linear system's behaviors are observed for relatively small perturbations.

4.4.2. Constrained vs unconstrained single MPC

To verify that the developed algorithm is working accurately, in this subsection, an MPC design problem is formulated and initially solved without any constraints on the actuators or on the states, and then the results are compared with the constrained case to observe the performance of the controller when there are small perturbations on its equilibrium Cartesian coordinates. For this purpose, the healthy OCT nonlinear model was linearized around the nominal solution corresponding to $U = 1.6$ m/s flow speed, and it was assumed that there was no change in the flow speed, i.e., F_p matrix in Eq. (14) is ineffective. The equilibrium states can be found in Table 6 with the equilibrium control inputs in Table 7. The linear model was perturbed 5 m in x and z, and -5 m in y positions. The system controlled by MPC was expected to return to the equilibrium point, which was set as the reference inside the controller. The results are shown in Fig. 6 for the position states. They clearly indicate that the system returns to the equilibrium z position in less than 10 s when there are no constraints applied (see the dash-dot blue line in Fig. 6). The other 10 states also return to the equilibrium values as desired. In Fig. 6 we also plot the results for the constrained case (see the dashed green line), as they are defined in Section 4.2. For this case, the system's settling time for

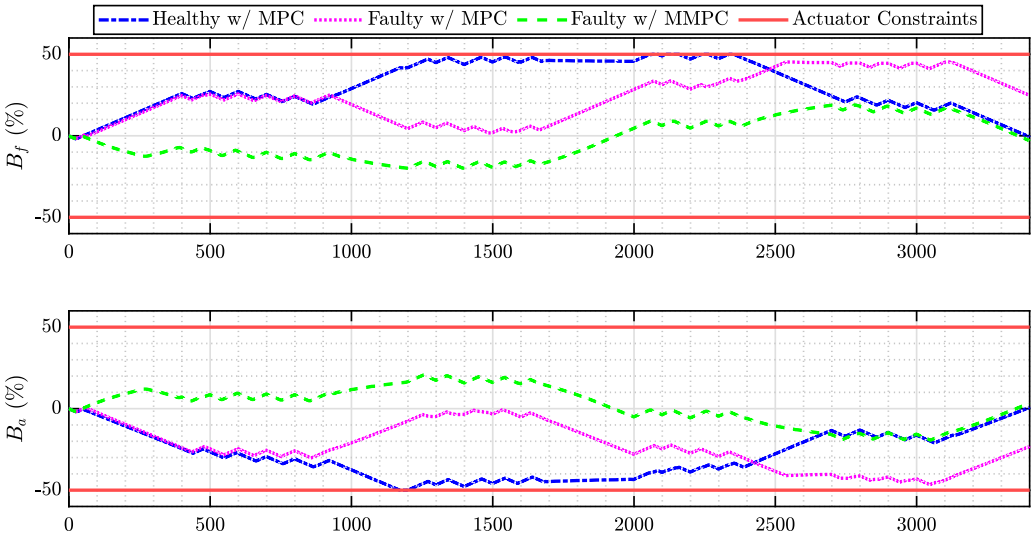

Fig. 13. Control inputs of the faulty & healthy OCT systems during the optimal trajectory following.

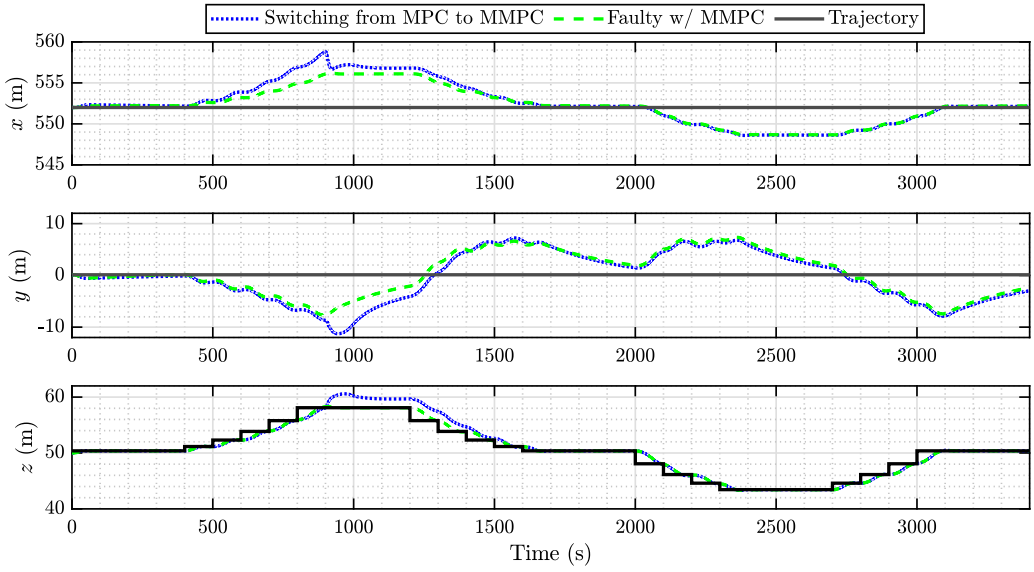

Fig. 14. Position states of the OCT systems to validate the robustness of the switching.

the z state is less than 200 s, indicating satisfactory performance for a heavy system like OCT. Besides the settling time, the system follows the reference with zero steady-state error after 800 s for all the states. Therefore, MPC provides the OCT system with high-accuracy reference tracking performance for multiple states with or without constraints.

In Fig. 7, the control inputs' time histories are plotted. For the unconstrained case, there were no constraints on the actuator in this MPC formulation, so control input values (dotted blue lines) do not obey the constraint limits defined in 4.2. From the unconstrained system's simulation, it can be observed that the buoyancy chamber fill fractions are the more effective actuators compared to the electromechanical shaft torque. Note that the constrained system's behavior is represented in green dashed lines, and they are in the limitations defined by the actuator constraints shown with the red solid lines. It indicates and verifies that the small perturbations can be eliminated with the hard constraints on the actuator inputs in a short period of time, as mentioned previously.

4.4.3. Reference tracking with a single MPC

In this subsection, we illustrate the capability of the MPC algorithm to maximize the power generation of the OCT by changing the operating water depth, z position. Specifically, the controller follows a prescribed depth (z position) variation and maintains the other states (x and y positions) constant (within acceptable tolerances). In this scenario, the MPC algorithm is tested on a given reference path for z that was ± 8 m from the equilibrium point.

In Fig. 8, one of the desired trajectories of the system and the simulation results for a healthy system are plotted. It can be seen that the reference tracking is achieved very well with the developed MPC, and the system was able to follow the desired path with less than 1 meter of steady-state error. In Fig. 9, the time histories of the control inputs that were applied to the system are shown. It can be seen that they do not violate the constraints that were defined in Eq. (42) and the control rate limitations are followed as defined in Eq. (43).

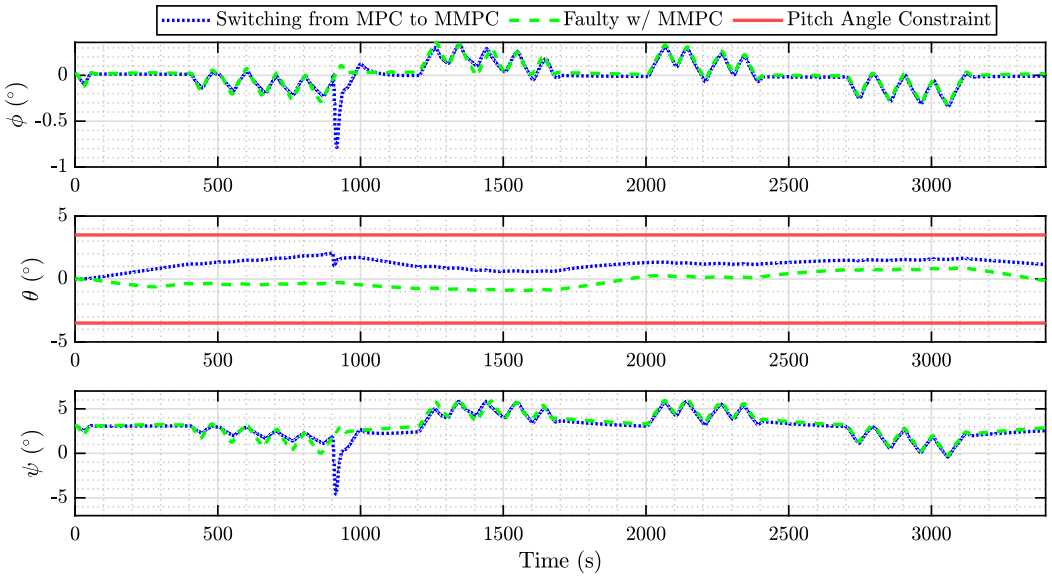

Fig. 15. Euler angles states of the OCT systems to validate the robustness of the switching.

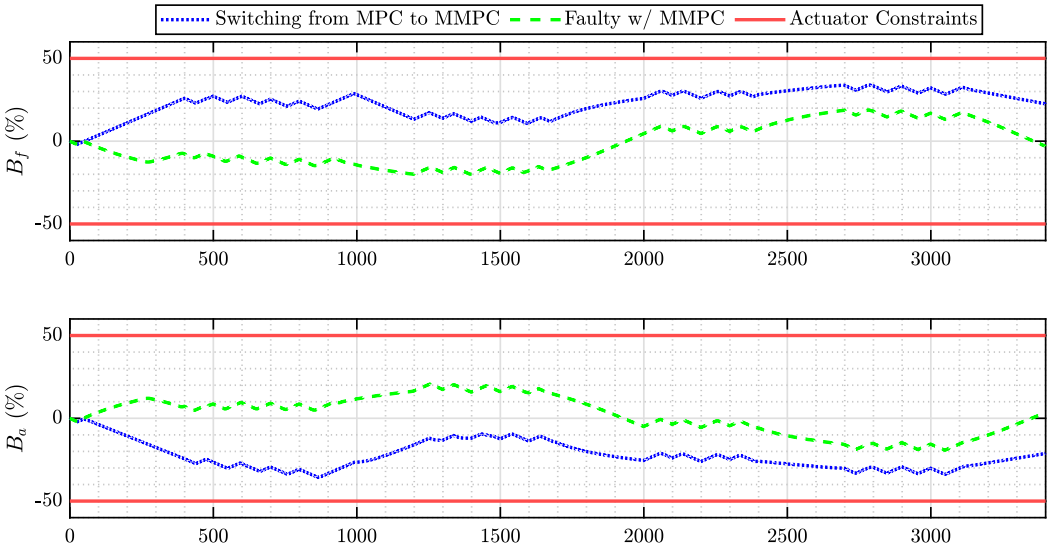

Fig. 16. Control inputs of the OCT systems to validate the robustness of the switching.

4.4.4. *Reference tracking of the faulty systems with MMPC controller*

In this case, the faulty system with the highest ν-gap value compared to the healthy system, $\beta_e = 10°$ as given in Table 2, was tested with different MPC structures to follow a reference trajectory for 1 h of operation, which was shown to be the optimal trajectory in Hasankhani et al. (2022b) and for comparison, the dash-dot blue line in Figs. 10–13 is the same MPC in that previous work. Inside the MPC block, the actuator constraints were enforced as defined in Section 4.2, and also the pitch angle was limited to 0.06 radians as required in the OCT design and operation. The ν−gap radius was chosen as 0.45 for the selected model set. For this radius value, in the model bank of the MMPC there are 8 models included, corresponding to β_e = 6°, 7°, 9°, 10°, 11°, 12°, 13°, 14°. In Fig. 10, the z position state was plotted, and the healthy system performance, dash-dot blue line, was compared with the faulty model controlled with a single MPC, dotted magenta line, and with the faulty model controlled with the proposed MMPC algorithm, dashed green line. The system performance decreases when there is a fault in one of the blades of the OCT; however, the MPC is still able to control it with an offset. It was desired to reach the optimal depth and keep the z position error of the OCT at a minimum to maximize the power generation and using the MMPC on the faulty system, the RMSE of z position was lowered from 1.3328 m to 0.7230 m, and that is even slightly better than the healthy case in which RMSE of z state was 0.7589 m.

In Fig. 11, all the position states were plotted. During the change of depth maneuvers, the OCT was moved in x and y axes, but since they were under 10 m, they were in acceptable margins for the system. The user-selected weights were assigned to maximize the power generation while keeping the computation time low as defined in Section 4.2, so these offsets in other axes than z were expected, and their effects on

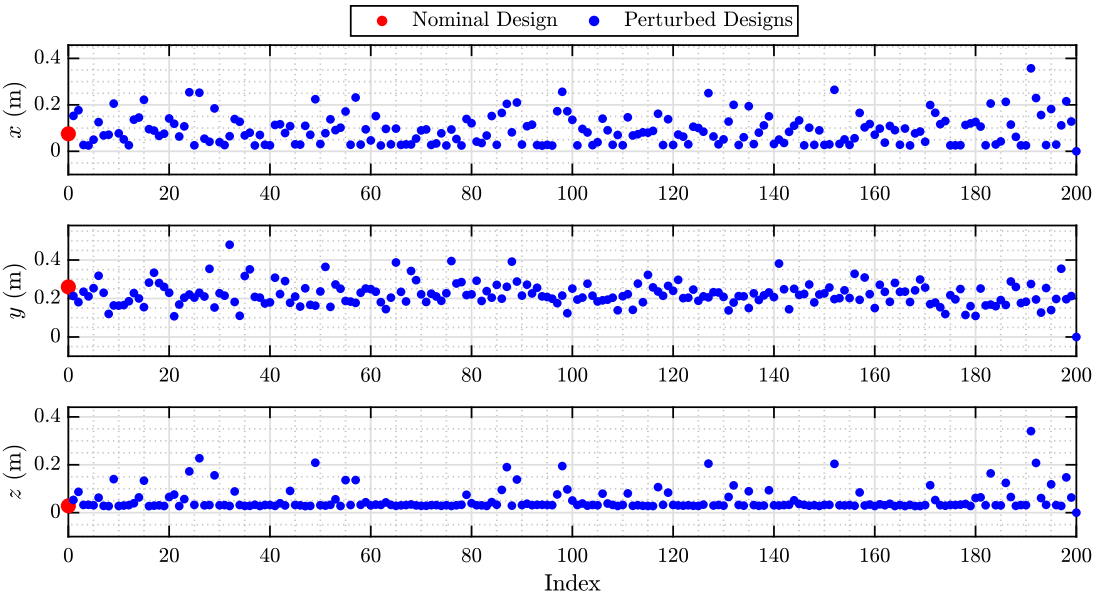

Fig. 17. Standard deviation of the position errors of the OCT systems.

the power generation were insignificant. In Fig. 12, the Euler Angles for 3 different scenarios were given. The pitch angle constraint, ±4°, was not violated throughout the simulation for all the cases, including the faulty system as desired, and the system was able to keep its attitude in the defined limits while it changed the depth, z, inside the ocean. The roll angle was fluctuating between ±0.5°, which was in very low magnitudes that can be neglected. The yaw angle had a change of ±3° which was an expected result of the linearization in which the restoring yaw moment of the system was eliminated. In the high-fidelity nonlinear model, that behavior would not occur, and since it was a low amount of offset from the desired target (i.e. 0° rotation around z-axis), the linear simulation results are in the acceptable margins. In Fig. 13, the control inputs were plotted with the actuator constraints. It is seen that the constraints were not violated throughout the operation in healthy or faulty cases as a result of using the MPC structure. Buoyancy chamber usage (B_f, B_a) was decreased on average, from 33% with the single MPC to 12% with MMPC, which was an additional benefit of using MMPC. On the other hand, the power generation increased by at least 18% with the MMPC on a faulty system (green dashed line) compared to a single MPC on a faulty system (dotted magenta line) according to the formulation given in Hasankhani et al. (2021b), as a result of following the desired depth reference with less error as mentioned previously. Therefore, the system was able to generate more power with less energy usage in the actuators during the faulty case when MMPC architecture was chosen. There was a drawback in computation time while using MMPC compared to single MPC, and the average computation time per iteration was increased almost 8 times, from 0.18 s to 1.35 s for Dell XPS 15 9570 computer, in which the lower time was for using the single MPC for a healthy system. MATLAB was chosen as the simulation environment in this work due to having the nonlinear model in Simulink, and this drawback can be eliminated with "Parallel Computing Toolbox" or by using other programming languages and optimization libraries. However, in this work, optimization of the algorithm speed (i.e. the computation time) was not within the scope of this paper and was instead considered an implementation issue. Therefore, it was out of the scope, and we focused on the development of the proposed algorithm that increases the power generation of the OCTs, rather than lowering the computational resource requirements of the algorithm.

4.4.5. Robustness analysis of the MMPC controller

In this section, two different robustness studies are presented. The first one investigates the effect of switching the model set used in controller design, to see if the switching structure of the MMPC controller leads to instability in the system. The second study is about the effect of parametric uncertainties in the system, to ascertain if the MMPC controller can achieve reference tracking sufficiently accurately under 10% uncertainty in the system matrix and input matrix parameters.

Switching Model Set Effect on MMPC Performance

To study the effect of switching, the following scenario was evaluated. A healthy plant that has no faults on the rotor blade pitch angle (i.e. $\beta_e = 0$), with a single MPC was considered. After the first 900 s, the plant model was changed to a 10-deg faulty model, and it was controlled by a single MPC designed using a healthy model for the next 600 s. This time interval is considered sufficient for the system to detect the magnitude of the fault in the rotor blades. At 1,500 s, it is assumed that the fault condition has been detected and characterized by a separate algorithm, and as a consequence, the controller is changed to an MMPC designed using 8 models within a ν-gap radius of 0.45, corresponding to $\beta_e = 6°,\ 7°,\ 9°,\ 10°,\ 11°,\ 12°,\ 13°,\ 14°$.

In Fig. 14, all the position states were plotted for this scenario. The switching scenario study is represented using a dotted blue line. It can be ascertained that switching from the single MPC to the MMPC did not result in any unstable behavior in any of the position states. This is an illustration of the fact that the control methodology proposed in this article is quite robust, even when dramatic switching (i.e. from single MPC to MMPC) is performed.

In Fig. 15, the Euler Angles for these two scenarios were given. Similar to the simulations in the previous sections, the pitch angle constraint, ±4°, was not violated throughout the simulation for the switching case, either. Right after the fault was applied in the simulation, there were sudden changes in the yaw and roll angles, but they did not exceed 5° and 1° respectively. This is an indication of very good performance of the proposed control scheme when switching occurs.

In Fig. 16, the control inputs were plotted with the actuator constraints depicted in red. The change of the model set in the controller design process did not cause any violation of the constraints. Moreover, the MMPC kept producing control inputs according to the slew rate changes. Again, this is an indication that the proposed control scheme has very good performance when switching occurs.

Effect of Parametric Uncertainty on MPC Performance

For the parametric uncertainty evaluation of the robustness, the following test was performed. All of the elements that are not 1 or 0 in the system matrices and the input matrices given in Appendix B were perturbed randomly by multiplying with a value in $[-1.10, 1.10]$. This is equivalent to perturbations within intervals of $\pm 10\%$ around the nominal values for all these elements. All the randomly perturbed systems were exponentially stable & controllable. Each perturbed system obtained in this manner was controlled by the nominal MPC to ensure accurate tracking of the optimal reference trajectory given previously. Fig. 17 shows the standard deviations of the position errors for the perturbed healthy system for 200 different cases randomly generated. It is seen that the position errors are close to the nominal design in all cases as they do not exceed 0.5 m. This indicates that the nominal design is robust with respect to uncertainties in OCT parameters.

5. Conclusion

A multi-model predictive control algorithm for nonlinear systems is proposed, and its effectiveness is presented with an application on an ocean current turbine system with pitch blade faults. The algorithm uses the ν-gap metric to identify the similarities of the models inside a model bank consisting of linear discrete-time models generated for different conditions from a high-fidelity, nonlinear model. This allows the user to control the system with an effective fault-tolerant method, and the MPC is defined for these systems in the form of a constrained quadratic program, so multiple states are controlled without violations on the defined constraints inside the optimization framework.

In the OCT application, the faults were isolated by making use of the ν-gap criteria for a given model bank. The control input to achieve the desired reference for the system, where the z position state is crucial to generate the maximum power inside the ocean, is aggregated from several linear models instead of using only one, and the control inputs are combined with a weight function defined on the basis of ν-gap metric. The controller obtains the control inputs to minimize the cost with the minimum amount of energy used in the actuators.

The proposed method provides a satisfactory trajectory following results for the OCT system, and with this proposed MMPC, even under faulty conditions, the system can be controlled in similar behavior to the single MPC case. This increases the power generated by the system significantly since the depth of the turbine is important to catch the highest flow speed inside the ocean. This approach can be used on other complex systems with multiple states, and if it were possible for the user to generate a model bank for different environmental conditions (or faults similar to our example case), MMPC would eliminate the performance differences that might have resulted from these different conditions.

Since it is a multi-model predictive control (MMPC), the implementation in a real system (embedded controller) is harder because of the complexity of the computations, which results in relatively high computation times. This was out of the scope of our paper, but it can be mitigated by using low-level programming languages instead of MATLAB and by making use of parallel computing toolboxes.

In future works, the implementation of the developed method in an experimental setup to test the algorithm under real-life conditions can be explored. For this, in addition to the MATLAB/Simulink simulation environment, other programming language options adequate for fast nonlinear simulations and experimental setup may be necessary. Also, instead of assuming that the fault is provided to the control framework by an external source, a more comprehensive framework can be developed by integrating the fault detection algorithm with the control algorithm. A long-term goal is to create a farm of OCTs that are interconnected in arrays through a local feed-in that sends generated power to a grid under different environmental conditions. The method developed and illustrated here is expected to be useful for the cooperative control framework for this farm to keep it operating during failures.

Table 3
Ocean current turbine system parameters.

Parameter	Symbol	Value
Rated power	P_{gen}	700 kW
Total mass (without the ballast water)	m	4.98×10^5 kg
Buoyancy chamber's water capacity	–	31.251 m^3
Moment of inertia of the entire system w.r.t. x-axis	I_x	1.35×10^7 kg m^3
Moment of inertia the entire system w.r.t. y-axis	I_y	4.74×10^7 kg m^3
Moment of inertia the entire system w.r.t. z-axis	I_z	3.45×10^7 kg m^3
Moment of inertia of the entire system w.r.t. xz plane	I_{xz}	-9.80×10^6 kg m^3
Ocean current speed	U	1.6 m/s
Rotor radius	–	20 m
Rotor airfoil	–	FX-83W
Mooring cable length	–	607 m
Mooring cable diameter	–	0.16 m
Generator efficiency	η_{gen}	0.98
Water pump efficiency	η_{pump}	0.75

CRediT authorship contribution statement

E. Baris Ondes: Conceptualization, Methodology, Software, Visualization, Writing – original draft. **Cornel Sultan:** Conceptualization, Validation, Writing – original draft, Supervision. **Arezoo Hasankhani:** Validation, Data curation, Writing – review & editing. **James H. VanZwieten:** Validation, Writing – review & editing, Supervision. **Nikolaos I. Xiros:** Writing – review & editing, Supervision.

Declaration of competing interest

The authors declare that they have no known competing financial interests or personal relationships that could have appeared to influence the work reported in this paper.

Data availability

Data will be made available on request.

Appendix A. System parameters

In this section, the parameters of the OCT system are tabulated in three different tables. In Table 3, the system parameters of the OCT are given, which are used in the high-fidelity nonlinear model, along with the dynamic equations of motion virtual parameters listed in Table 4. And in Table 5, the constraints are provided for the actuator and also for the pitch angle limit of the OCT, which are used in the model predictive control framework.

Appendix B. Stable linear OCT models data

In this section, the numerical values of the two stable CLTI models are given. In following subsections, system matrices, $A_{p,i}$, input matrices, $B_{p,i}$, and the flow matrices, $F_{p,i}$, are listed separately. As mentioned in Section 2.4, the output matrices, $C_{p,i}$ are identity matrices of 12×12.

Table 4
Dynamic equations of motion virtual parameters.

Parameter	Symbol	Value
Virtual mass of the entire system	m^v	4.98×10^5 kg
Virtual mass of the main body	m_b^v	4.36×10^5 kg
Virtual mass of the rotor	m_r^v	6.16×10^4 kg
Virtual distance of the body from the center of gravity in z axis	$z_{G_b}^v$	−2.49 m
Virtual distance of the entire system from the center of gravity in x axis	x_G^v	6.51 m
Virtual moment of inertia of the entire system w.r.t. x-axis	I_x^v	1.35×10^7 kg m^3
Virtual moment of inertia of the entire system w.r.t. y-axis	I_y^v	4.74×10^7 kg m^3
Virtual moment of inertia of the entire system w.r.t. z-axis	I_z^v	3.45×10^7 kg m^3
Virtual moment of inertia of the entire system w.r.t. xz plane	I_{xz}^v	-9.80×10^6 kg m^3
Virtual moment of inertia of the main body w.r.t. x-axis	$I_{x_b}^v$	1.30×10^7 kg m^3
Virtual moment of inertia of the main body w.r.t. y-axis	$I_{y_b}^v$	4.62×10^7 kg m^3
Virtual moment of inertia of the main body w.r.t. z-axis	$I_{z_b}^v$	3.34×10^7 kg m^3
Virtual moment of inertia of the main body w.r.t. xz plane	$I_{xz_b}^v$	-9.80×10^6 kg m^3
Virtual moment of inertia of the rotor w.r.t. x-axis	$I_{x_r}^v$	5.39×10^6 kg m^3
Virtual moment of inertia of the rotor w.r.t. y-axis	$I_{y_r}^v$	1.15×10^6 kg m^3
Virtual moment of inertia of the rotor w.r.t. z-axis	$I_{z_r}^v$	1.15×10^6 kg m^3

$$A_{p,1} = \begin{bmatrix}
-0.31491 & -0.079839 & -0.0034405 & -0.21682 & -0.49486 & 0.19637 & 0.029143 & 2.5939e{-}05 & -0.024974 & 0.0071045 & -0.83916 & -0.011334 \\
0.00016831 & -0.14103 & 0.60903 & 0.27299 & 1.5342 & 2.1564 & -1.1136e{-}05 & -8.8582e{-}05 & 1.5579e{-}05 & 1.2291 & -0.063045 & 0.31007 \\
-0.077123 & -0.4697 & -0.17188 & -0.059573 & -1.0222 & 1.2104 & 0.011597 & 8.1511e{-}06 & -0.01094 & 0.0033554 & -3.5767 & -0.046007 \\
9.9918e{-}05 & -0.048285 & -0.0040622 & -0.65355 & -0.020593 & -0.38215 & -2.57e{-}05 & -0.0002044 & 3.5948e{-}05 & -1.6596 & -0.0044995 & 0.19277 \\
-0.011835 & -0.044001 & -0.0019493 & -0.0091395 & -0.30809 & 0.10806 & 7.889e{-}05 & 1.3596e{-}06 & 0.00052729 & -0.0002676 & -0.60244 & -0.0064492 \\
-1.6543e{-}05 & 0.010637 & -0.06426 & 0.0046065 & -0.15236 & -0.37469 & 2.5361e{-}05 & 0.0002017 & -3.5473e{-}05 & 0.27403 & 0.01049 & -0.13504 \\
-1 & 0.0015468 & -0.00038862 & 0 & 0 & 0 & 0 & 0 & 0 & 0 & 0 & 0 \\
-0.0015513 & -0.99993 & 0.012019 & 0 & 0 & 0 & 0 & 0 & 0 & 0 & 0 & 0 \\
-0.00037 & 0.01202 & 0.99993 & 0 & 0 & 0 & 0 & 0 & 0 & 0 & 0 & 0 \\
0 & 0 & 0 & 1 & 4.4473e{-}06 & 0.00036997 & 0 & 0 & 0 & 0 & 0 & 0 \\
0 & 0 & 0 & 0 & 0.99993 & -0.01202 & 0 & 0 & 0 & 0 & 0 & 0 \\
0 & 0 & 0 & 0 & 0.01202 & 0.99993 & 0 & 0 & 0 & 0 & 0 & 0
\end{bmatrix} \tag{B.1}$$

Box I.

$$A_{p,2} = \begin{bmatrix}
-0.35342 & -0.087492 & 0.042654 & -0.10161 & 0.26711 & 0.21704 & 0.03157 & 2.8762e{-}06 & -0.015506 & 0.0054306 & -1.4937 & -0.013491 \\
-0.013203 & -0.13488 & 0.65311 & 0.26671 & 1.7607 & 2.0998 & -1.5849e{-}05 & -1.9864e{-}05 & 8.3908e{-}06 & 1.111 & -0.030719 & 0.24846 \\
-0.086037 & -0.45273 & -0.15423 & -0.022706 & -0.65578 & 1.2382 & 0.023098 & 4.5005e{-}08 & -0.01198 & 0.0073945 & -4.5193 & -0.02233 \\
0.011887 & -0.02478 & -0.0018493 & -0.60359 & -4.5306e{-}05 & -0.41491 & -0.00023346 & -0.00029258 & 0.00012359 & -1.6043 & -0.0038454 & 0.17225 \\
-0.018081 & -0.039829 & 0.0050952 & -0.0038632 & -0.13721 & 0.1038 & 0.0016424 & 5.9774e{-}07 & -0.00066859 & 0.0014121 & -0.7215 & -0.0027226 \\
-0.0022936 & 0.0013295 & -0.070047 & -0.012768 & -0.17995 & -0.24681 & 0.0001968 & 0.00024664 & -0.00010418 & 0.3674 & 0.0062107 & -0.11699 \\
-0.9998 & -0.020009 & -0.0011137 & 0 & 0 & 0 & 0 & 0 & 0 & 0 & 0 & 0 \\
0.019991 & -0.9997 & 0.014325 & 0 & 0 & 0 & 0 & 0 & 0 & 0 & 0 & 0 \\
-0.0014 & 0.014299 & 0.9999 & 0 & 0 & 0 & 0 & 0 & 0 & 0 & 0 & 0 \\
0 & 0 & 0 & 1 & 2.0019e{-}05 & 0.0013999 & 0 & 0 & 0 & 0 & 0 & 0 \\
0 & 0 & 0 & 0 & 0.9999 & -0.0143 & 0 & 0 & 0 & 0 & 0 & 0 \\
0 & 0 & 0 & 0 & 0.0143 & 0.9999 & 0 & 0 & 0 & 0 & 0 & 0
\end{bmatrix} \tag{B.2}$$

Box II.

Table 5
The constraint values of the actuator and the OCT system.

Parameter	Symbol	Value
Buoyancy chambers' fill fraction upper/lower limit	$B_{\text{aft,front}}$	±50%
Buoyancy chambers' fill fraction rate limit	$\dot{B}_{\text{aft,front}}$	7.45×10^{-6} %/s
Pitch angle limit	θ_{lim}	±4°

Also, the equilibrium states and equilibrium control inputs are given in Tables 6 and 7 in the last subsection.

$A_{p,1}$ and $A_{p,2}$ indicate the system matrices for non-faulty system with 0° fault, and faulty system with 10° fault, respectively. The rest of the systems' can be accessed via Elsevier's system as a .mat file see Box II.

B.1. System matrices

See (B.1) and (B.2) given in Boxes I and II.

B.2. Input matrices

$$B_{p,1} = \begin{bmatrix}
0.0053155 & -0.085709 \\
-0.0014029 & -0.0069603 \\
-0.23781 & -0.56429 \\
-0.0017502 & -0.0020574 \\
0.0028751 & -0.047255 \\
0.00022988 & 0.0011689 \\
0 & 0 \\
0 & 0 \\
0 & 0 \\
0 & 0 \\
0 & 0 \\
0 & 0
\end{bmatrix} \tag{B.3}$$

Table 6
Equilibrium states of the systems.

Fault	u_{eq} [m/s]	v_{eq} [m/s]	w_{eq} [m/s]	$p_{b,eq}$ [RPM]	q_{eq} [RPM]	r_{eq} [RPM]	x_{eq} [m]	y_{eq} [m]	z_{eq} [m]	ϕ_{eq} [°]	θ_{eq} [°]	ψ_{eq} [°]
0°	0	0	0	0	0	0	554.50	0.38	50.00	0.01	0	3.14
1°	0	0	0	0	0	0	555.43	1.68	49.98	0.01	0	3.15
2°	0	0	0	0	0	0	555.10	1.53	49.99	0.01	0	3.15
3°	0	0	0	0	0	0	554.77	1.38	50.00	0.01	0	3.15
4°	0	0	0	0	0	0	554.77	1.38	50.00	0.01	0	3.15
5°	0	0	0	0	0	0	554.07	0.99	49.99	0.01	0	3.14
6°	0	0	0	0	0	0	553.69	0.81	50.02	0.01	0	3.14
7°	0	0	0	0	0	0	553.30	0.70	50.06	0	0.01	3.15
8°	0	0	0	0	0	0	552.88	0.58	50.04	0	0.01	3.14
9°	0	0	0	0	0	0	552.46	0.46	50.01	0.01	0	3.13
10°	0	0	0	0	0	0	552.00	0.12	49.99	0.01	0	3.12
12°	0	0	0	0	0	0	551.01	−0.05	49.92	0.02	−0.01	3.13
14°	0	0	0	0	0	0	549.91	0.25	49.93	0.02	−0.02	3.13
16°	0	0	0	0	0	0	549.19	0.99	49.91	0.02	−0.02	3.13
18°	0	0	0	0	0	0	548.28	1.90	50.01	0	0	3.16
20°	0	0	0	0	0	0	547.59	2.43	50.13	−0.02	0.02	3.14

$$B_{p,2} = \begin{bmatrix} 0.022536 & -0.12099 \\ -0.0007714 & -0.01127 \\ -0.24971 & -0.67796 \\ -0.0023701 & -0.0028203 \\ 0.010123 & -0.055635 \\ 0.00021967 & 0.0019826 \\ 0 & 0 \\ 0 & 0 \\ 0 & 0 \\ 0 & 0 \\ 0 & 0 \\ 0 & 0 \end{bmatrix} \quad \text{(B.4)}$$

B.3. Flow matrices

$$F_{p,1} = \begin{bmatrix} -0.42206 & 0.0060561 & 0.0081731 \\ 0.0003522 & -0.16482 & 0.041211 \\ -0.10656 & 0.029329 & 0.18804 \\ 0.00017033 & -0.049688 & 0.0018471 \\ -0.016329 & 0.003523 & 0.0045047 \\ -2.4735e{-}05 & 0.014743 & -0.005861 \\ 0 & 0 & 0 \\ 0 & 0 & 0 \\ 0 & 0 & 0 \\ 0 & 0 & 0 \\ 0 & 0 & 0 \\ 0 & 0 & 0 \end{bmatrix} \quad \text{(B.5)}$$

$$F_{p,2} = \begin{bmatrix} -0.37732 & 0.0079343 & 0.0090169 \\ -0.019442 & -0.15101 & 0.019164 \\ -0.09016 & 0.014195 & 0.16577 \\ 0.015927 & -0.036805 & 0.00095416 \\ -0.013935 & 0.0015682 & 0.0033856 \\ -0.0032198 & 0.013455 & -0.0026623 \\ 0 & 0 & 0 \\ 0 & 0 & 0 \\ 0 & 0 & 0 \\ 0 & 0 & 0 \\ 0 & 0 & 0 \\ 0 & 0 & 0 \end{bmatrix} \quad \text{(B.6)}$$

B.4. Equilibrium states and control inputs

See Tables 6 and 7.

Table 7
Equilibrium control inputs of the systems.

Fault	$B_{f,eq}$ [%]	$B_{f,eq}$ [%]
0°	47	47
1°	25	71
2°	24	71
3°	23	70
4°	21	70
5°	20	69
6°	18	69
7°	17	68
8°	16	68
9°	14	67
10°	13	67
12°	10	66
14°	8	65
16°	6	64
18°	5	63
20°	4	63

References

Altman, A., Gondzio, J., 1999. Regularized symmetric indefinite systems in interior point methods for linear and quadratic optimization. Optim. Methods Softw. 11 (1–4), 275–302. http://dx.doi.org/10.1080/10556789908805754.

Bryden, H.L., Beal, L.M., Duncan, L.M., 2005. Structure and transport of the Agulhas Current and its temporal variability. J. Oceanogr. 61 (3), 479–492.

Coiro, D., Troise, G., Scherillo, F., De Marco, A., Calise, G., Bizzarrini, N., 2017. Development, deployment and experimental test on the novel tethered system GEM for tidal current energy exploitation. Renew. Energy 114, 323–336.

Du, J., Johansen, T.A., 2014. A gap metric based weighting method for multimodel predictive control of MIMO nonlinear systems. J. Process Control 24 (9), 1346–1357. http://dx.doi.org/10.1016/j.jprocont.2014.06.002.

El-Sakkary, A.K., 1985. The gap metric: Robustness of stabilization of feedback systems. IEEE Trans. Automat. Control 30 (3), 240–247. http://dx.doi.org/10.1109/TAC.1985.1103926.

Fossen, T.I., 2011. Rigid-body kinetics. In: Handbook of Marine Craft Hydrodynamics and Motion Control. John Wiley & Sons, Ltd, pp. 45–58. http://dx.doi.org/10.1002/9781119994138.ch3.

Freeman, B., Tang, Y., Huang, Y., VanZwieten, J., 2021. Rotor blade imbalance fault detection for variable-speed marine current turbines via generator power signal analysis. Ocean Eng. 223, 108666. http://dx.doi.org/10.1016/j.oceaneng.2021.108666.

Freeman, B., Tang, Y., Huang, Y., VanZwieten, J., 2022. Physics-informed turbulence intensity infusion: A new hybrid approach for marine current turbine rotor blade fault detection. Ocean Eng. 254 (November 2021), 111299. http://dx.doi.org/10.1016/j.oceaneng.2022.111299.

Freeman, B., Tang, Y., VanZwieten, J., 2019. Marine hydrokinetic turbine blade fault signature analysis using continuous wavelet transform. In: 2019 IEEE Power Energy Society General Meeting. PESGM, pp. 1–5. http://dx.doi.org/10.1109/PESGM40551.2019.8973470.

Greer, W.B., Sultan, C., 2020. Shrinking horizon model predictive control method for helicopter–ship touchdown. J. Guid. Control Dyn. 43 (5), 884–900. http://dx.doi.org/10.2514/1.G004374.

Haas, K., 2013. Assessment of energy production potential from ocean currents along the United States coastline. Technical report, Georgia Inst. of Technology, Atlanta, GA (United States).

Hasankhani, A., Huang, Y., VanZwieten, J., Tang, Y., 2022a. Real-time vertical path planning using model predictive control for autonomous marine current turbine. In: 2022 Conference on Control Technology and Applications (CCTA).

Hasankhani, A., Ondes, E.B., Tang, Y., Vanzwieten, J., 2022b. Integrated path planning and tracking control of marine current turbine in uncertain ocean environments. In: 2022 American Control Conference. ACC, pp. 3106–3113.

Hasankhani, A., Tang, Y., VanZwieten, J., Sultan, C., 2021a. Comparison of deep reinforcement learning and model predictive control for real-time depth optimization of a lifting surface controlled ocean current turbine. In: 2021 IEEE Conference on Control Technology and Applications. CCTA, IEEE, pp. 301–308. http://dx.doi.org/10.1109/CCTA48906.2021.9659089, URL https://ieeexplore.ieee.org/document/9659089/.

Hasankhani, A., Tang, Y., VanZwieten, J., Sultan, C., 2022c. Spatiotemporal optimization for vertical path planning of an ocean current turbine. IEEE Trans. Control Syst. Technol. 1–15. http://dx.doi.org/10.1109/TCST.2022.3193637.

Hasankhani, A., VanZwieten, J., Tang, Y., Dunlap, B., De Luera, A., Sultan, C., Xiros, N., 2021b. Modeling and numerical simulation of a buoyancy controlled ocean current turbine. Int. Mar. Energy J. 4 (2), 47–58. http://dx.doi.org/10.36688/imej.4.47-58.

Intelligent and Resilient Energy Systems (IRES) Research Group, 2021. Buoyancy controlled ocean current turbine numerical modeling. http://dx.doi.org/10.5281/zenodo.5035867, URL https://github.com/IRES-FAU/Buoyancy-Controlled-Ocean-Current-Turbine-Modeling.

Jerri, A., 1977. The Shannon sampling theorem—Its various extensions and applications: A tutorial review. Proc. IEEE 65 (11), 1565–1596. http://dx.doi.org/10.1109/PROC.1977.10771.

Jiang, D., Huang, Q., Hong, L., 2009. Theoretical and experimental study on wind wheel unbalance for a wind turbine. In: 2009 World Non-Grid-Connected Wind Power and Energy Conference. pp. 1–5. http://dx.doi.org/10.1109/WNWEC.2009.5335787.

Lund, D.C., Lynch-Stieglitz, J., Curry, W.B., 2006. Gulf stream density structure and transport during the past millennium. Nature 444 (7119), 601–604.

Mikhailov, N.N., 2002. Russian Marine Expeditionary Investigations of the World Ocean. Vol. 5, US Department of Commerce, National Oceanic and Atmospheric Administration.

Navy, U.S., 2008. Submarine Trim and Drain Systems. Periscope Film, LLC, pp. 3–19.

Ngo, T.D., Sultan, C., VanZwieten, J.H., Xiros, N.I., 2017. Model predictive control for moored ocean current turbines. In: 2017 American Control Conference. ACC, pp. 875–880. http://dx.doi.org/10.23919/ACC.2017.7963063.

Ngo, T.D., Sultan, C., VanZwieten, J.H., Xiros, N.I., 2021. Constrained control of moored ocean current turbines with cyclic blade pitch variations. IEEE J. Ocean. Eng. 46 (2), 594–610. http://dx.doi.org/10.1109/JOE.2020.2985599.

Pham, H.-T., Bourgeot, J.-M., Benbouzid, M.E.H., 2018. Comparative investigations of sensor fault-tolerant control strategies performance for marine current turbine applications. IEEE J. Ocean. Eng. 43 (4), 1024–1036. http://dx.doi.org/10.1109/JOE.2017.2747018.

Radanovic, B., Driscoll, F., 2002. Development of an efficient general purpose cable model and simulation for marine applications. In: Oceans '02 MTS/IEEE. Vol. 4, IEEE, pp. 2060–2067. http://dx.doi.org/10.1109/OCEANS.2002.1191949, URL http://ieeexplore.ieee.org/document/1191949/.

Rentschler, M.U., Adam, F., Chainho, P., 2019. Design optimization of dynamic inter-array cable systems for floating offshore wind turbines. Renew. Sustain. Energy Rev. 111 (September 2018), 622–635. http://dx.doi.org/10.1016/j.rser.2019.05.024.

Sato, A., Kanoh, H., Takagi, K., 2021. Control of a twin-turbine submerged floating system in turbulent flow. Ocean Eng. 225, 108769. http://dx.doi.org/10.1016/j.oceaneng.2021.108769.

Ueno, T., Nagaya, S., Shimizu, M., Saito, H., Murata, S., Handa, N., 2018a. Development and demonstration test for floating type ocean current turbine system conducted in kuroshio current. In: 2018 OCEANS - MTS/IEEE Kobe Techno-Oceans. OTO, pp. 1–6. http://dx.doi.org/10.1109/OCEANSKOBE.2018.8558792.

Ueno, T., Nagaya, S., Shimizu, M., Saito, H., Murata, S., Handa, N., 2018b. Development and demonstration test for floating type ocean current turbine system conducted in kuroshio current. In: 2018 OCEANS-MTS/IEEE Kobe Techno-Oceans. OTO, IEEE, pp. 1–6.

Vanderbei, R.J., Carpenter, T.J., 1993. Symmetric indefinite systems for interior point methods. Math. Program. 58 (1), 1–32.

Vanrietvelde, N., 2009. Numerical performance prediction for FAU's first generation ocean current turbine. (Master's thesis). Florida Atlantic University, Boca Raton.

VanZwieten, J., Driscoll, F., Leonessa, A., Deane, G., 2006. Design of a prototype ocean current turbine—Part II: flight control system. Ocean Eng. 33 (11), 1522–1551. http://dx.doi.org/10.1016/j.oceaneng.2005.10.006.

VanZwieten, J.H., Pyakurel, P., Ngo, T., Sultan, C., Xiros, N.I., 2016. An assessment of using variable blade pitch for moored ocean current turbine flight control. Int. J. Mar. Energy 13, 16–26. http://dx.doi.org/10.1016/j.ijome.2016.01.002.

VanZwieten, J.H., Vanrietvelde, N., Hacker, B.L., 2013. Numerical simulation of an experimental ocean current turbine. IEEE J. Ocean. Eng. 38 (1), 131–143. http://dx.doi.org/10.1109/JOE.2012.2218891.

Vinnicombe, G., 1993. Frequency domain uncertainty and the graph topology. IEEE Trans. Automat. Control 38 (9), 1371–1383. http://dx.doi.org/10.1109/9.237648.

Vinnicombe, G., 1999. A /spl nu/-gap distance for uncertain and nonlinear systems. In: Proceedings of the 38th IEEE Conference on Decision and Control (Cat. No.99CH36304). Vol. 3, pp. 2557–2562. http://dx.doi.org/10.1109/CDC.1999.831313.